

Mechanical Performance of Amorphous Metallic Cellular Structures

Thesis by
Joseph P. Schramm

In Partial Fulfillment of the Requirements
for the Degree of
Doctor of Philosophy



California Institute of Technology
Pasadena, California

2010

(Defended October 9, 2009)

© 2010

Joseph P. Schramm

All Rights Reserved

Acknowledgements

First of all, I would like to thank my advisor, Professor William Johnson, for his guidance and inspiring ideas. In the last 6 years, because of Professor Johnson, I have never lacked ideas to test out in the laboratory. I would like to thank Professor Dale Conner, who was the first person to show me around and introduce me to the lab and has been a great collaborator and friend. I would like to thank Dr. Marios Demetriou, who has been a somewhat difficult person to collaborate with, but as a result has helped me to truly understand our research and always brings the best science out of the data. Other members of the Johnson group have been great friends and colleagues. I have shared office space with Dr. Chris Veazey, Dr. John Harmon, and Annelen Kahl, each of whom was willing to put up with my bad jokes and taste for loud, noisy, or generally weird music. I have also shared an office with Glenn Garrett, with whom I have shared plenty of eccentric music and an obsession with delicious food. Georg Kaltenboeck has been an outstanding research assistant and a great guy to have around. I am also quite grateful to so many other members of the Johnson group and the Fultz group who have made the 3rd floor of Keck such an enjoyable and interesting place to work.

When I was a kid, I used to say I wanted to be a scientist. Now that I can consider myself a scientist, I need to thank my family for allowing that to happen and for supporting me unconditionally through the last 29+ years. My parents raised my brothers and me to think for ourselves and to be good people, and I think they did a fantastic job. My brothers and I have always been great friends and through their respective graduate studies, we have celebrated breakthroughs, commiserated over difficulties, and shared opinions on music and the Chicago Bears and politics and just about anything else you could think of.

For the last four years, my wife Jane has dealt with me as a boyfriend, as a roommate, as a fiancé, and now, as a husband. She has been as kind and supportive as anyone could hope for. Jane is my best friend, and making it through the last four years of life and graduate school without her could not possibly have been as fulfilling.

Abstract

Metallic glass and metallic glass matrix composites are excellent candidates for application in cellular structures because of their outstanding plastic yield strengths and their ability to deform plastically prior to fracture. The mechanical performance of metallic-glass and metallic-glass-matrix-composite honeycomb structures are discussed, and their strength and energy absorption capabilities examined in quasi-static compression tests for both in-plane and out-of-plane loading. These structures exhibit strengths and energy absorption that well exceed the performance of similar structures made from crystalline metals. The strength and energy absorption capabilities of amorphous metal foams produced by a powder metallurgy process are also examined, showing that foams produced by this method can be highly porous and are able to inherit the strength of the parent metallic glass and absorb large amounts of energy. The mechanical properties of a highly stochastic set of foams are examined at low and high strain rates. It is observed that upon a drastic increase in strain rate, the dominant mechanism of yielding for these foams undergoes a change from elastic buckling to plastic yielding. This mechanism change is thought to be the result of the rate of the mechanical test approaching or even eclipsing the speed of elastic waves in the material.

Contents

1	Introduction	1
2	Metallic Glass Honeycombs	8
3	Metallic Glass Matrix Composite Honeycombs	29
4	High Porosity Metallic Glass Foam: A Powder Metallurgy Route	46
5	The Effect of Strain Rate on the Yielding Mechanism of Amorphous Metal Foams	58
6	Summary and Future Directions	70
	Bibliography	75

List of Figures

2.1	Schematic representation of the stress-strain curves of cellular structures in quasi-static compression (from Gibson and Ashby [24]).	9
2.2	Stress-strain response of porous Pd-based bulk metallic glass (from Wada and Inoue [29]).	10
2.3	Differential calorimetry scans of (a) a feedstock amorphous rod, (b) a corrugated sheet, (c) a sheet etched for 8 minutes, and (d) a corrugated sheet re-equilibrated at 380°C for 2 minutes. The glass transition temperature for each scan is indicated with an arrow, and the enthalpy change shown is that for crystallization.	16
2.4	Forming die, amorphous feedstock rod, and amorphous corrugated sheet.	18
2.5	(a) Single core as prepared for mechanical testing. The z-axis is the in-plane loading axis, and the x-axis is the out-of-plane loading axis. (b) Assembled stack of four cores with grooved stainless steel horizontal plates with relative density $\rho^* = 0.074$	18

2.6	(a) Stress-strain response of quasi-statically loaded single cores of corrugated metallic glass of varying relative density. (b) Comparison of stress-strain behavior of BMG core and Steel core of nearly the same relative density. Steel data from Côté et al. [46].	20
2.7	Images of a single core during compression testing: (a) elastic region, (b) yielding, (c) after first collapse event, and micrographs of the specimen after compression showing (d) macroscopic plastic deformation and (e) shear bands on the tension surface of the strut, two of which are indicated with white arrows.	20
2.8	Stress-strain response of quasi-statically loaded multi-core stacks of corrugated metallic glass with relative densities of (a) 0.084, (b) 0.142, and (c) 0.169.	22
2.9	(a) Stress-strain response of three out-of-plane quasi-statically loaded metallic glass cores. (b) Comparison of stress-strain behavior of BMG core and Steel core of nearly the same relative density. Steel data from Côté et al. [47].	24
2.10	Images showing a metallic glass corrugation loaded in compression: (a) in the elastic region, (b) after the first collapse event showing failure that spans several struts at an angle of roughly 45° to the axis of loading, and (c) after several collapse events. (d) A corrugation with $\rho^*/\rho_s = 0.105$ whose struts were thin enough to buckle, and (e) a micrograph of a specimen after out-of-plane compression showing a failure along a single shear band.	24

2.11	Relative strength-relative density plot for metallic glass structures tested in-plane and out-of-plane. Lines are power law best fits to the data.	25
2.12	Strength-relative density relation for metallic glass and stainless steel cores (closed symbols) and stacks (open symbols) compressed (a) in-plane and (b) out-of-plane. Lines are power law best fits through the data. Steel data from ref. [46, 47]. . .	26
2.13	Stress-strain curve for a stack of metallic glass cores showing calculation of energy absorbed (shaded area).	27
2.14	Energy absorption diagram for metallic glass cores and stacks and stainless steel structures in (a) in-plane and (b) out-of-plane loading. Lines are power law best fits through the data.	28
3.1	(a) XRD of as forged corrugation verifying phase character of the metallic glass matrix composite showing amorphous background and indexed bcc crystal peaks (from Hofmann et al. [23]). (b) Image of metallic glass matrix composite as prepared for quasi-static compression. The z-axis is the in-plane loading axis, and the x-axis is the out-of-plane loading axis. .	32
3.2	Stress-strain response of (a) single cores and (b) two-core stacks of MGMC corrugated sheets for quasi-static in-plane loading and (c) single cores in quasi-static out-of-plane loading. . . .	33
3.3	Images of a single core of the MGMC (a) in the elastic region, (b) after the first collapse event, and (c) near densification, and electron micrographs of a specimen after compression showing (d) severe plastic deformation and (e) a dense network of shear bands in the area of severe plastic deformation.	34

3.4	Images of a two-core stack of the MGMC (a) in the elastic region, (b) after the first collapse event showing that the nodes of the two cores are now misaligned, and (c) further deformation of the structure showing that the plastic deformation is not uniform across the structure.	35
3.5	Images of out-of-plane MGMC specimens during testing (a) in the elastic region and (b) showing plastic buckling in the plateau after yielding and (c) top view after the first collapse event. Electron micrographs of an out-of-plane MGMC specimen: (d) side view showing massive deformation along large shear bands and (e) shear bands on top compression surface.	36
3.6	Images of an MGMC egg-box structure (a) as prepared for testing and (b) after testing showing the ability to flatten almost completely and remain largely in one piece. (c) Stress-strain response of a representative egg-box with $\rho^*/\rho_s=0.12$	38
3.7	Relative strength-relative density plot for MGMC structures in in-plane and out-of-plane loading. Lines are power law best fits to the data.	39
3.8	Stress-strain plots comparing the behavior of MGMC structures with steel structures of roughly the same density and similar geometry for (a) in-plane honeycomb, (b) out-of-plane honeycomb, and (c) egg-box structures. Steel data from refs. [46, 47]	41
3.9	Strength-relative density plots for BMG and MGMC structures and crystalline metal structures under (a) in-plane and (b) out-of-plane loading. Steel and aluminum data from refs. [46, 47]	42

3.10	Energy absorbed per unit mass versus relative density plots for BMG and MGMC structures and crystalline metal structures under (a) in-plane and (b) out-of-plane loading. Steel data from refs. [46, 47]	43
3.11	Energy absorbed per unit mass versus plateau stress for MGMC structures and crystalline metal structures showing very high energy absorption capabilities of MGMC structures. Steel data from ref. [46].	44
4.1	Differential calorimetry scans of the metallic glass powder (a), the precursor (b), and the foam (c). Arrow in (b) indicates a minor bump associated with the endothermic decomposition reaction of the agent.	49
4.2	Image of an 82% porosity foam produced via the introduced powder metallurgy route, alongside a precursor segment of equivalent mass. Inset: X-ray diffractogram verifying the amorphous nature of the foam.	51
4.3	Scanning electron micrographs showing the microstructure of the precursor (a) and (b), and the cellular structure of an 82% foam (c) and (d).	53
4.4	Compressive stress-strain diagrams of 4% (a), 40% (b), and 86% (c) porosity foams. Inset: Foam relative strengths plotted against relative densities. The solid line is a plot of the power law correlation established for plastically yielding foams [24].	55
4.5	Compressive stress-strain diagram of an 86% porosity foam deformed toward full densification.	56

5.1	(a) Image of a foam specimen as prepared for dynamic compression. (b) Image of a foam specimen after dynamic compression showing several completely densified pieces among other crushed pieces. (c),(d) Electron micrographs of a completely densified piece of a dynamically compressed foam. . . .	61
5.2	Dynamic stress-strain response of foams with varying relative densities (reported in percent porosity) under strain rates between 3000 s^{-1} and 3500 s^{-1}	63
5.3	A comparison of the stress-strain response of two 60% porosity foams under applied strain rates of 3500 s^{-1} and $1 \times 10^{-4} \text{ s}^{-1}$. .	65
5.4	Relative strength as a function of relative density for foams tested under low and high applied strain rates. The inset shows a comparison between quasi-static ($\sim 10^{-4} \text{ s}^{-1}$) and dynamic (10^3 s^{-1}) compression of aluminum foams (Ref. [66]). Solid lines are power-law fits to the data.	67
6.1	Examples of crystalline metal (a) textile and (b) truss.	72

Chapter 1

Introduction

Bulk Metallic Glasses

The first metallic glass, discovered in 1960 as a result of studies on rapidly cooled metals, was a $\text{Si}_{25}\text{Au}_{75}$ alloy that was rapidly quenched against a spinning copper wheel at $\sim 10^6$ K/s into flakes about 10 μm thick, which were found to be unstable as an amorphous structure at room temperature for times longer than a few hours [1]. Since this discovery, amorphous metals have been the subject of a great deal of research that has resulted in a multitude of glass-forming alloys in many alloy systems including, but not limited to, the Pd-Si-based ternaries studied by Chen and Turnbull [2], the Zr-Al-(Ni-Cu) and Pd-Ni-Cu-P alloys of the Inoue group [3, 4], and the Zr-Ti-based beryllium-containing (Vitreloy) alloys developed by the Johnson group of Caltech [5, 6].

A glass is a solid that has been formed without undergoing the discontinuous solidification of crystallization. The solidification of a glass happens continuously as the liquid becomes more and more viscous until the liquid is essentially solid, that is the liquid is viscous enough that the time required for a rearrangement of the positions of the atoms in the liquid is significantly greater than the laboratory timescale [7]. This transition from liquid to glass

is called the glass transition and happens at a temperature called the glass transition temperature, T_g , defined as the temperature at which the liquid has a viscosity of 10^{12} Pa-s. At this viscosity (for $T = T_g$), Vitreloy 1, an exemplary glass-forming alloy has a structural relaxation time of ~ 100 s [8] which means that it would take about 2 minutes to observe any flow with no externally applied stress. At lower and lower temperatures, the relaxation time would continue to increase making the alloy appear essentially solid. A glass can be formed as long as this transition can happen without crystallization of the liquid.

The rate at which a liquid must be cooled in order to successfully avoid crystallization can be inferred from time-temperature-transformation diagram (TTT) for crystallization. The lowest cooling rate at which the nose of the TTT is still avoided is called the critical cooling rate. The lowest critical cooling rate ever measured for an amorphous metal is 0.005 K/s, which was measured in dispersed droplets of $\text{Pd}_{43}\text{Ni}_{10}\text{Cu}_{27}\text{P}_{20}$ [9]. The critical cooling rate for bulk $\text{Pd}_{43}\text{Ni}_{10}\text{Cu}_{27}\text{P}_{20}$ has been measured to be 0.09 K/s [10]. Low critical cooling rates allow a glass-forming alloy to be formed with large dimensions. An alloy with similar composition, $\text{Pd}_{40}\text{Ni}_{10}\text{Cu}_{30}\text{P}_{20}$, has been formed into fully amorphous specimens with minimum dimension as large as 72 mm [11]. The development of many bulk glass-forming alloys (those that can be formed >1 mm thick) has allowed for thorough study of the properties of these materials.

Metallic glasses have a unique set of mechanical properties including high strength and elasticity, broadly varying toughness, and lack of ductility [12]. For example, bulk metallic glasses have remarkably high yield strengths, σ_y , (up to ~ 2 GPa) [13], large elastic limits (near 2% strain), a wide range of fracture toughness, K_c , (ranging from $2 \text{ MPa}\sqrt{m}$ to nearly $100 \text{ MPa}\sqrt{m}$) [14], and effectively zero ductility in tension at room temperature. Metallic glasses

can, however, show some plasticity in more stable loading conditions like compression [15] and bending [16]. Bending is an interesting loading configuration for metallic glass because it combines compression, where uniaxially tested metallic glasses can show plasticity, and tension, where they show none. When a plate of metallic glass is bent so that the surface stresses exceed the yield stress of the material, shear bands will form at the surface. The shear band spacing and the distance the shear bands will travel toward the neutral axis is determined by the thickness and curvature of the sample. In thinner samples (equal to or thinner than the plastic zone size, $d = K_c^2/(\pi\sigma_{ys}^2)$) the shear bands travel shorter distances and, therefore, have smaller offsets resulting in lower chance of a crack nucleating from a shear band, so a thin sample will yield plastically [16, 17].

These mechanical properties are the direct consequence of the amorphous structure of metallic glasses. Unlike crystalline metals, the atoms in an amorphous metal are arranged in a more or less randomly, that is, there is no long-range order so no line defects, like dislocations, are possible. In crystalline metals, dislocation motion is the main method of deformation, and plastic deformation increases the density of dislocations, which causes a macroscopic strain hardening. Because of this lack of crystalline order, dislocations are not present in metallic glasses, so metallic glasses have strengths closer to theoretical strength than any other bulk metals, but this also leaves no strain hardening mechanism. Metallic glasses actually exhibit strain softening at room temperature which results in inhomogeneous flow upon yielding which manifests itself as narrow regions of plastic deformation referred to as shear bands. When a specimen of metallic glass is loaded uniaxially, plastic deformation generally restricted to few shear bands, and the ultimate failure generally occurs along one dominant shear band oriented along a plane of maximum shear $\sim 45^\circ$ to the axis of loading. When metallic glasses do ex-

hibit plasticity, it is due to the formation of multiple shear bands [18].

Metallic glasses bridge the gap in toughness between ceramics and metals, and can exhibit very brittle or quite ductile behavior. Recently, much research has been focused on understanding the physics of metallic glasses and what makes some glasses less prone to brittle failure. In examining fracture toughness and fracture energy Lewandowski et al. realized that the intrinsic toughness of a metallic glass is related to Poisson's ratio, ν , for the material. A transition from low fracture energy to high fracture energy is observed as ν increases beyond ~ 0.32 [14]. Attempts have been made to produce metallic glasses with high Poisson's ratio and, consequently, greater toughness and plasticity with varying degrees of success [9, 19, 20, 21]. Another method of toughening metallic glass is to produce a composite consisting of a metallic glass matrix and another (usually softer) interspersed phase. The most successful metallic glass matrix composites have been *in situ* composites made by precipitating a low shear modulus dendrite phase in the liquid alloy prior to quenching. These composites exhibit ductility in tension and very high toughness [22, 23].

As a result of the extraordinary mechanical properties and the recent breakthroughs in the toughening of metallic glasses, there is ongoing interest in the use of metallic glasses as engineering materials. Because of the remarkably high yield strengths and potential for high toughness, these materials are attractive candidates for use as the parent material in very strong cellular structures with high energy absorption capabilities.

Cellular Solids

Ranging from natural materials like wood, cork, and bone to advanced engineering materials like impact-absorbing car bumpers, heat exchangers, and

lightweight building panels, cellular solids have many uses. Cellular solids can be fabricated in many different geometries which can be separated into two different categories: aperiodic structures, as in the case of foams, and periodic structures, like honeycombs and trusses. Each geometry lends a distinct set of properties to the structure. These materials have been thoroughly studied over the last three decades and their properties are fairly well understood [24, 25].

Engineered cellular solids are usually designed to meet the specific needs of an application. The cellular structures examined in this thesis are designed to be strong and light and capable of absorbing large amounts of energy. High strength structures with good energy absorbing capabilities should be made from a high strength parent material and should be designed so that the walls or struts of the structure can be loaded to the yield strength of the parent material without buckling elastically and the structures should maintain a considerable and constant stress level over a wide range of strain. In order to achieve this, the parent material should be able to undergo significant plastic deformation before fracture occurs. Elastic buckling is avoided by designing cell walls and struts to have slenderness smaller than a critical slenderness ratio for buckling. Brittle failure of metallic glass is avoided by producing struts and walls that are thinner than the plastic zone size of the parent material.

Chapters 2 and 3 of this thesis deal with the design, fabrication, and testing of honeycomb-like structures made from bulk metallic glass (BMG) and metallic glass matrix composites (MGMC), respectively. To date, periodic cellular structures made of metallic glass or its composites have not been seen in the literature. Periodic structures made from crystalline metals, on the other hand have been available commercially for several decades and their mechanical properties have been well characterized [26, 27]

The mechanical properties of cellular solids are determined by several factors including cellular geometry, the properties of the parent material and, in the case of the strength capabilities of a structure, the dominant yielding mechanism of the cellular elements, and follow general semi-empirical relationships of the type developed by Gibson and Ashby [24]:

$$\frac{\sigma^*}{X_s} \simeq C \left(\frac{\rho^*}{\rho_s} \right)^n, \quad (1.1)$$

where σ^* is the yield strength of the cellular solid, X_s is the relevant scaling property of the parent material, C is a scaling coefficient that comes from the geometry of the cells, and n is an exponent determined by the geometry of the structure and the mechanics of the cell walls. The measured properties of the cellular structures in this thesis will be compared to semi-empirical relationships of this type. This comparison with established correlations can show whether the cellular solid has inherited the desirable properties of the parent metallic glass. Further discussion of the origin of these relationships can be found in chapter 2.

Only recently have metallic glasses been utilized as the parent material for any cellular solid. Amorphous metal foams have been the subject of much study over the last 6 years, and can be made by several methods, including thermoplastic expansion after melting in the presence of a blowing agent [28], melting and casting in the presence of a high pressure gas [29], infiltration over a place-holding preform [30] or hollow spheres [31], and co-extrusion of powders with a fugitive phase followed by dissolution of that phase [32]. A honeycomb-like structure with unidirectional pores has also been produced by casting over then electrochemically etching away wires of a fugitive phase [33].

These amorphous metal foams have been shown to have a collection of

mechanical properties not previously seen in porous materials. Amorphous metals with small amounts of porosity have been shown to have very high strengths and exhibit significantly more plasticity than monolithic specimens [29]. Structures with lower relative densities, specifically those comprised of struts thinner than the plastic zone size of the amorphous metal, have been found to be extremely deformable, as catastrophic failure due to global brittle fracture is effectively avoided [30, 34]. Highly stochastic foams comprised of struts with broadly varying thicknesses and aspect ratios have been shown to yield by elastic buckling [35]. When amorphous metal foams are produced with thin struts and uniform aspect ratios, they can avoid both brittle fracture and elastic buckling to yield plastically at rather low relative densities (<10%) [36]. Consequently, these foams are among the strongest foams ever seen.

Chapter 4 discusses the fabrication of high porosity amorphous metal foam by a powder metallurgy method and the excellent mechanical properties of these foams, and chapter 5 is concerned with the yielding mechanism of the aforementioned highly stochastic amorphous metal foams and the effect of strain rate on the yielding mechanism.

Chapter 6 summarizes the work in this thesis and proposes some interesting continuing research on the processing and mechanical performance of metallic glass and metallic glass matrix composite structures.

Chapter 2

Metallic Glass Honeycombs

Introduction

Due to the fact that they undergo a glass transition and are stable as an undercooled liquid over a large range of temperatures for a significant amount of time, some metallic glasses have the ability to be formed like plastics. In this vein, metallic glasses can be formed independently from the rapid quenching necessary to avoid crystallization unlike die casting or other forms of casting from the liquid state. The thermoplastic properties of metallic glasses have been utilized to create blow-molded parts [37], extrusions of consolidated powders [38], and foams [39] for instance. A series of bulk metallic alloys has been developed for thermal stability and thermoplastic formability having supercooled liquid regions greater than 150°C and casting thicknesses exceeding 15 mm [40]. Recently, it has been shown that one of these metallic glasses ($\text{Zr}_{35}\text{Ti}_{30}\text{Be}_{27.5}\text{Cu}_{7.5}$) has a relatively low viscosity in the supercooled liquid region, and therefore, can be plastically formed by injection molding while maintaining the high strength expected from metallic glass [41].

Metallic glasses have also been used to make several types of cellular structures including high strength foams which are capable of inheriting the me-

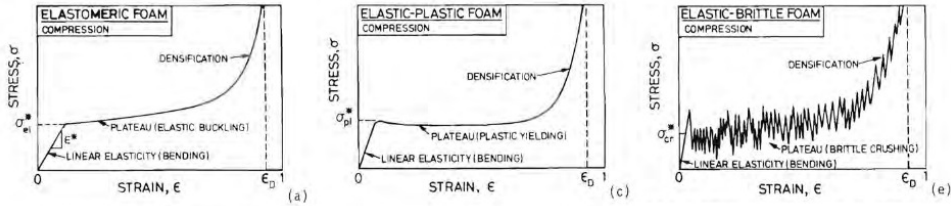


Figure 2.1: Schematic representation of the stress-strain curves of cellular structures in quasi-static compression (from Gibson and Ashby [24]).

chanical properties of the parent metallic glass [36, 42], and metallic glasses with directional porosity [43] or uniaxial porosity [33]. This chapter deals with the fabrication and testing of corrugated sheets and honeycomb structures made by thermoplastic forming of a bulk metallic glass.

Mechanics of Cellular Solids

Schematic stress-strain curves for cellular solids made from different types of materials are shown in figure 2.1 (from reference [24]). Structures with struts yielding by each mechanism exhibit the same general stress-strain behavior with slightly different shapes. Elastic and plastic yielding both show a smooth yielding transition followed by a long, flat stress plateau. Unlike an elastically yielding structure, a plastically yielding structure shows a stress peak before the plateau. The stress-strain curve of a structure whose elements fail by brittle fracture is very rough, showing a sharp peak and a plateau made of many non-catastrophic collapse events. Foams made of metallic glass have been shown to be capable of yielding plastically, but they still exhibit many non-catastrophic collapse events [36]. An example stress-strain foam curve showing this plastic yielding followed by collapse event behavior is reproduced from Wada and Inoue [29] in figure 2.2.

As discussed in chapter 1, the mechanical properties of cellular solids

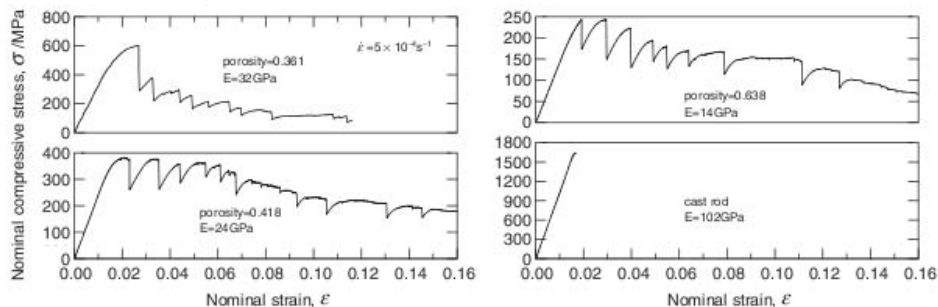


Figure 2.2: Stress-strain response of porous Pd-based bulk metallic glass (from Wada and Inoue [29]).

are determined by several factors including cellular geometry, the properties of the parent material, and the mechanics of the cellular elements in the structure. The strength capabilities of cellular solids follow general semi-empirical relationships of the type:

$$\frac{\sigma^*}{X_s} \simeq C \left(\frac{\rho^*}{\rho_s} \right)^n. \quad (2.1)$$

Following the analysis of Gibson and Ashby [24] for uniaxial in-plane loading of low density honeycombs, equating the load on a strut due to a remote stress with the critical load for buckling gives a yield strength relation for elastic buckling.

$$\frac{\sigma^*}{E_s} \simeq C_1 \left(\frac{\rho^*}{\rho_s} \right)^3. \quad (2.2)$$

Equating the surface stress caused by the resultant moment of a remote stress on the structure with the modulus of rupture of the brittle material gives a relation for elastic-brittle cellular solids.

$$\frac{\sigma^*}{\sigma_{fs}} \simeq C_2 \left(\frac{\rho^*}{\rho_s} \right)^2. \quad (2.3)$$

Equating the maximum moment in the beam due to a remote stress with the

fully plastic moment of the cell wall in bending gives a relation for elastic-plastic cellular solids.

$$\frac{\sigma^*}{\sigma_{ys}} \simeq C_3 \left(\frac{\rho^*}{\rho_s} \right)^2. \quad (2.4)$$

The most important factors in these equations are the material property scaling factors, which largely determine the magnitude of σ^* , and the exponents, which determine how σ^* changes with the relative density. The material scaling properties are especially important as they vary over orders of magnitude with E usually in tens of GPa while σ_{fs} and σ_{ys} range from hundreds of MPa up to several GPa.

The values of the three coefficients (C_1 , C_2 , and C_3) come from the geometry and mechanics of the analyzed structure. Equations 2.3 and 2.4 differ in the values of their coefficients and the scaling. Examining these coefficients, C_3 is always larger than C_2 because the fully plastic moment in a cellular element,

$$M_p = \frac{1}{4} \sigma_{ys} b t^2, \quad (2.5)$$

where b is the depth of the honeycomb and t is the thickness of a strut, is always smaller than the moment required to cause the surface stress of an element to reach the brittle fracture stress, σ_{fs} ,

$$M_f = \frac{1}{6} \sigma_{fs} b t^2, \quad (2.6)$$

so if two parent materials, one with σ_{fs} which equals σ_{ys} of the other, the structure that fails by brittle crushing will always have a lower yield stress than the structure that fails by plastic yielding. When experimentally measured relative strengths are plotted against relative density, the results can be compared to the relations presented in equations 2.2 through 2.4 to help in determining the failure mechanism of the cellular solid.

In the case of out-of-plane compressive loading, the elements of the struc-

ture are aligned with the axis of loading, resulting in higher relative strengths as the struts are loaded uniaxially instead of in bending, so the strength-porosity relations are somewhat changed. The out-of-plane properties of honeycombs are not as thoroughly studied, so the strength-porosity relations for these loading conditions are largely empirical. Again, following Gibson and Ashby [24], honeycombs that buckle elastically still have an exponent of $n = 3$ in out-of-plane loading, but the coefficient should be significantly higher (~ 20 times higher) than for in-plane loading. Out-of-plane loading for elastic-brittle honeycombs results in a linear relationship between relative strength and relative density which should be a one-to-one relationship if σ_{fs} is measured in compression. On first observation, it would appear that the same would be true for elastic-plastic honeycombs, but the situation is a bit more complex for most honeycombs as the struts tend to undergo plastic buckling. If a honeycomb were to yield plastically without plastic buckling, the relation should be one-to-one. Thorough analysis of this plastic buckling in cell walls by Wierzbicki [44] has shown that minimizing the collapse load with respect to the wavelength of the plastic buckling yields an exponent of $n = 5/3$ in the strength-porosity relationship for out-of-plane plastic collapse of honeycombs.

As described here, the highest relative strengths attainable are those for structures whose elements yield plastically. Metallic glasses in bulk sizes fail by global brittleness, and thin columns are quite susceptible to elastic buckling because of their high elastic limit, but are capable of yielding plastically without catastrophic brittle failure under certain circumstances. As a result of these properties, metallic glass cellular structures can be vulnerable to these less desirable mechanisms of failure, and therefore the design of the structure is critical in optimizing the properties of a metallic glass cellular structure.

To avoid elastic buckling, a structure should contain struts that have slenderness below a critical ratio which can be calculated from the Euler equation for buckling.

$$P_{cr} = \frac{n^2\pi^2 EI}{L^2}, \quad (2.7)$$

$$\sigma_{cr} = \frac{P_{cr}}{A} = \frac{n^2\pi^2 EI}{AL^2} = \frac{n^2\pi^2 E}{(L/r)^2}. \quad (2.8)$$

Set $\sigma_{cr} = \sigma_{ys}$ to get critical slenderness ratio for buckling:

$$\left(\frac{L}{r}\right)_{cr} = n\pi\sqrt{\frac{E}{\sigma_{ys}}}. \quad (2.9)$$

Using $E=95$ GPa and $\sigma_{ys} = 1750$ MPa for $Zr_{35}Ti_{30}Be_{29}Co_6$

$$\left(\frac{L}{r}\right)_{cr} \simeq 23n, \quad (2.10)$$

n varies between $\frac{1}{2}$ and 2 depending on end conditions, so the critical slenderness ratio varies between roughly 10 and 50.

For metallic glasses, brittle fracture is the dominant failure mechanism, but plastic yielding preempts brittle fracture in bending when the thickness of a cell wall is thinner than the plastic zone size for the alloy. As a result of these design constraints, the structures studied in this chapter were designed to have struts 5 mm long with thickness of 0.5 mm or less. This keeps the struts at the low end of the range of critical slenderness ratios and thin enough that they should yield plastically before fracture.

Another important property of a cellular structure is its ability to absorb energy as it is deformed. Cellular solids absorb energy during deformation by turning mechanical energy into another type of energy (usually thermal energy). This can happen by plastic deformation of the solid or by friction between broken cell walls and struts, as is the case for cellular solids that un-

dergo brittle failure. The energy absorbed per unit volume can be calculated from a stress-strain curve:

$$W = \int_0^\varepsilon \sigma(\varepsilon) d\varepsilon, \quad (2.11)$$

which is the area under the stress-strain curve up to ε . Ideally, an energy absorbing structure should have an elastic region, where cell walls bend elastically, followed by an extended plateau with relatively constant stress over a large strain, where energy is absorbed by plastic yielding or brittle fracture, ending in densification as seen in the generalized stress-strain curves in figure 2.1 for three different mechanisms of failure [24]. The majority of the energy absorbed by a cellular structure is absorbed in the plateau region, so maintaining a relatively high and relatively constant plateau stress is important. The rapid increase in stress at densification is due to the fact that the structure has collapsed to the point where the cell walls begin to be pressed against each other. When calculating the useful energy absorbed from a stress-strain curve for a cellular structure, the integral is usually carried out to the densification strain, ε_D , because beyond that point, the experiment is directly testing the behavior of the parent material, and not the cellular structure.

Methods

Ingots of a $\text{Zr}_{35}\text{Ti}_{30}\text{Be}_{29}\text{Co}_6$ glass-forming alloy were formed by arc melting in a gettered argon atmosphere using elements of >99.9% purity. This alloy was chosen for its large supercooled liquid region ($\sim 150^\circ\text{C}$) and its high critical casting thickness (which is slightly higher than the injection molded $\text{Zr}_{35}\text{Ti}_{30}\text{Be}_{27.5}\text{Cu}_{7.5}$ alloy mentioned above). From these ingots, amorphous rods with 6 mm diameter were vacuum induction cast using a copper mold.

The amorphous nature of these cast rods was verified using differential scanning calorimetry (DSC) as shown in figure 2.3(a). Using two aligned steel dies and a heated 50-ton hydraulic press, amorphous rods were heated to 430°C (T_g+100) as measured by an attached thermocouple, then pressed until the applied load reached a predetermined limit (usually 48–50 tons). At this temperature and load, the corrugated sheets end up with struts that are 5 mm long and 0.6–0.4 mm thick. The entire die assembly was subsequently water quenched. The entire process was carried out in ambient air and was completed in ~ 3 minutes.

Because the forming occurred in ambient air, the surface of the corrugated sheets shows some signs of oxidation, but this appears not to affect the amorphous nature of the corrugated sheets which was also verified using DSC as seen in figure 2.3(b). The forming die, a feedstock amorphous rod and an amorphous corrugated sheet are shown in figure 2.4. The die was designed so that the adjacent struts were at a 60° angle to each other resulting in an equilateral triangle honeycomb-type structure. The amorphous corrugated sheets were cut into strips approximately 5 mm by 35 mm so that the long axis was perpendicular to the ridges in the sheets. Initial mechanical tests resulted in an undesirable brittle failure, so the sheets were heated to 50°C above the calorimetric T_g , held for 2 minutes to equilibrate and quenched in an attempt to capture a higher energy (higher Poisson's ratio) configuration of the glass. DSC of a representative re-equilibrated specimen is shown in figure 2.3(c). In order to achieve a range of low relative densities, some specimens were then thinned using a stirred solution of 45 mL HNO_3 :10 mL HF :45 mL H_2O . The HF/HNO_3 solution removed material rather quickly (struts thinned at a rate of approximately 20 μm per minute), but the mass loss appeared macroscopically uniform, and the thinned material remains glassy. A thermal scan of an etched specimen is shown in figure 2.3(d). The thermal analysis shows

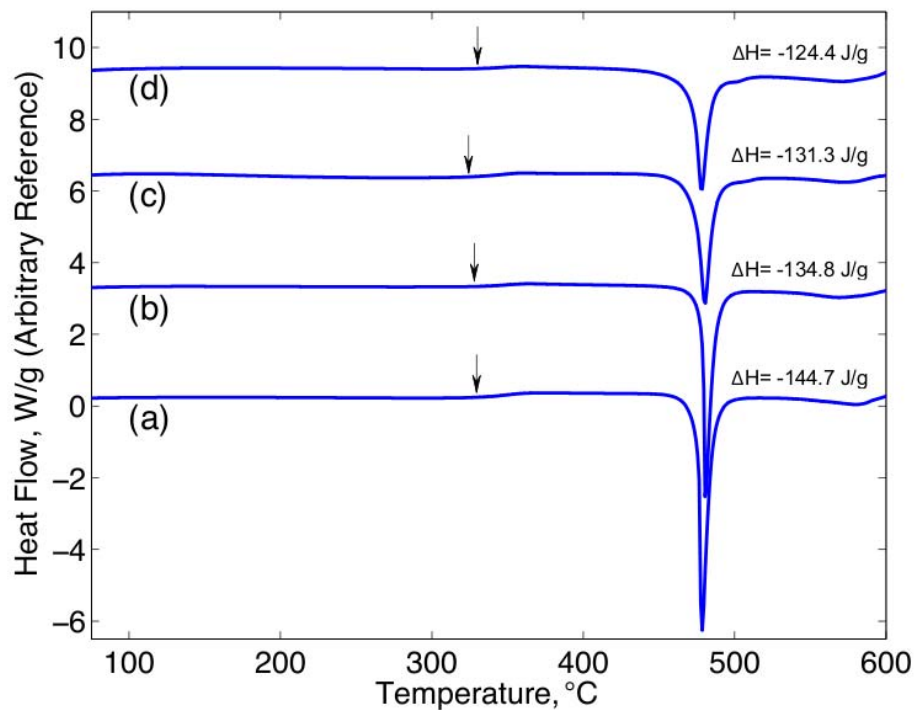


Figure 2.3: Differential calorimetry scans of (a) a feedstock amorphous rod, (b) a corrugated sheet, (c) a sheet etched for 8 minutes, and (d) a corrugated sheet re-equilibrated at 380°C for 2 minutes. The glass transition temperature for each scan is indicated with an arrow, and the enthalpy change shown is that for crystallization.

that while T_g and T_x remain relatively constant, while each subsequent processing step slightly reduces the enthalpy of crystallization. This decrease in ΔH through the processing of a corrugated sheet is about 20 J/g.

The nature of this change in enthalpy of crystallization is not known, but there are several possible explanations. The first, and simplest is that the glass has been partially crystallized. In other Zr-based, Be-bearing metallic glasses, partial crystallization has been observed to cause embrittlement resulting in a severe drop in toughness from $\sim 50 \text{ MPa}\sqrt{m}$ to $\sim 5 \text{ MPa}\sqrt{m}$ [45]. The structural integrity of these cores and the evidence of plastic deformation discussed below imply that the material is probably not embrittled. Another possibility is that the processing has lowered the configurational enthalpy of the structure. The extra enthalpy in the glass is the product of the ΔC_p between the liquid and the glass and the difference in the temperature from which the glass was quenched. (For the cast rod this is somewhere above the calorimetric T_g , and for the corrugations it is the annealing temperature.) A third possible explanation for this change in enthalpy is the possibility of a phase separation in the glass during the processing steps. A phase separation into two glasses would be an irreversible spinodal type of transformation that would lower the enthalpy of the system resulting in a lower observed enthalpy of crystallization.

These corrugated strips were tested in the in-plane configuration, the z-axis direction in figure 2.5(a), as single cores and as stacks. In both cases, each core was sandwiched between grooved stainless steel plates, each groove corresponding to a node of the corrugation. These plates serve as a means for aligning and confining the nodes of the cores. The stacks were assembled using epoxy, which serves only to hold the stack together prior to mechanical testing. An example of a single core and a multi-core stack are shown in figure 2.5(a) and (b). Single cores were also tested in out-of-plane configuration,

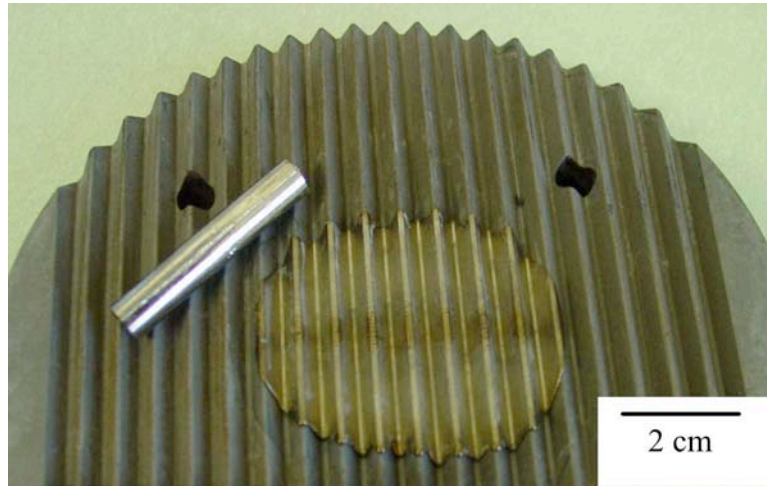


Figure 2.4: Forming die, amorphous feedstock rod, and amorphous corrugated sheet.

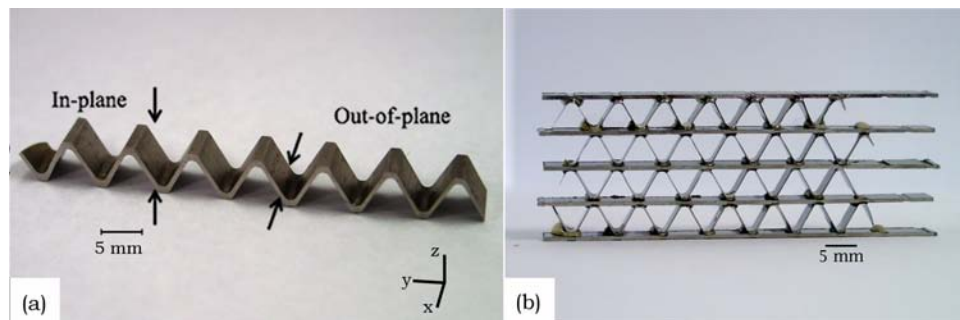


Figure 2.5: (a) Single core as prepared for mechanical testing. The z-axis is the in-plane loading axis, and the x-axis is the out-of-plane loading axis. (b) Assembled stack of four cores with grooved stainless steel horizontal plates with relative density $\rho^* = 0.074$

the x-axis direction in figure 2.5(a), between flat steel plates. Prior to testing, the cut surfaces were ground flat and parallel. All specimens were compressed quasi-statically with an applied strain rate of 10^{-3}s^{-1} . Tests were carried out with a screw-driven Instron universal testing machine with a load capacity of 50 kN and displacements were measured with a linear variable differential transformer. The relative density of the specimens was calculated using the known geometry of the forming die and the average measured thickness of the struts in a core or stack. The thicknesses of the struts varied by about $\pm 15\%$ from the average measured thickness.

Results

In-Plane Loading

The stress-strain response of quasi-statically loaded single cores is shown in figure 2.6(a). Images of a representative sample during a compression test are shown in figure 2.7(a) through (c). The stress-strain curves typically show an elastic region followed by a short period of plastic deformation leading to a peak in stress. This peak is followed by a substantial stress drop, then a rather low but relatively constant stress plateau. These single cores show significantly higher yield strength than a steel structure of nearly the same relative density (figure 2.6(b)) while maintaining a comparable plateau stress after yielding. Figure 2.7(b) shows that the metallic glass exhibits a significant amount of deformation before the first failure event. Once the first failure event has occurred, the core is still capable of holding load, and portions of the specimen have undergone severe plastic deformation, as can be seen in figure 2.7(c). Micrographs of compressed specimens seen in figure 2.7(d) and (e) also show macroscopic evidence of plastic deformation and shear bands on the tension surface of one strut.

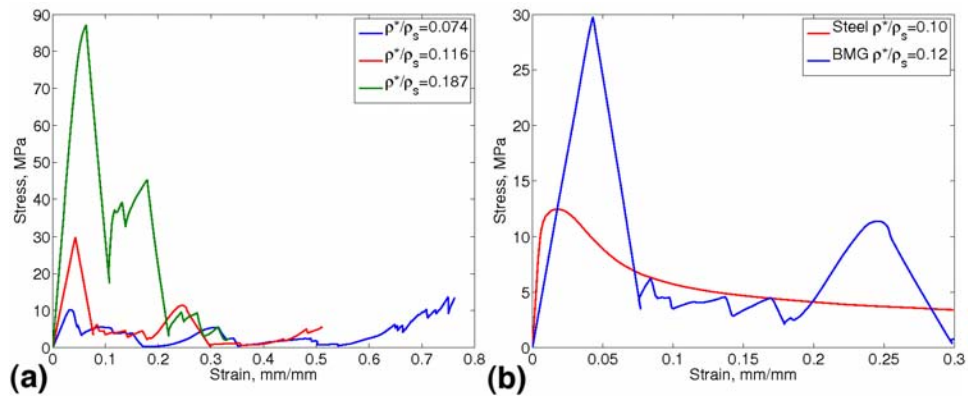


Figure 2.6: (a) Stress-strain response of quasi-statically loaded single cores of corrugated metallic glass of varying relative density. (b) Comparison of stress-strain behavior of BMG core and Steel core of nearly the same relative density. Steel data from Côté et al. [46].

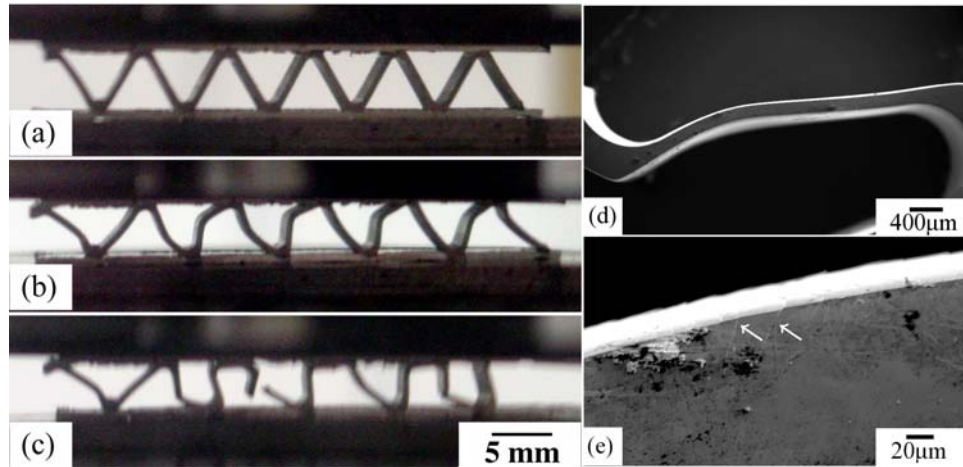


Figure 2.7: Images of a single core during compression testing: (a) elastic region, (b) yielding, (c) after first collapse event, and micrographs of the specimen after compression showing (d) macroscopic plastic deformation and (e) shear bands on the tension surface of the strut, two of which are indicated with white arrows.

The severe stress drop and low plateau stress seen in the single core tests are believed to be a result of the fact that each specimen is composed of around ten struts, therefore, each strut is a critical member, and the fracture of one strut has a quite catastrophic effect on the behavior of the entire core. As seen in figure 2.7(c), the first collapse event in these single cores causes significant rearrangement of the remaining struts which results in a significant reduction in the stability of the structure. One would assume that a structure with more layers or merely more struts would result in a smaller stress drop and a higher plateau stress because fracture of one strut is accommodated by a larger number of remaining struts. The stress-strain response of multi-core stacks, seen in figure 2.8, shows that a structure with more struts actually does show a higher stresses throughout the plateau than do single cores. The curves in figure 2.8(a) and (b) do show a significant stress drop, however, it is followed by a gradually increasing plateau to densification. Upon closer inspection of the stress-strain response in figure 2.6(a) and figure 2.8, there are five or six significant collapse events, each one probably corresponding to the collapse of a single strut, before the onset of densification for the single cores, while the stacked cores with about 30 or 40 struts show around 20 significant collapse events prior to densification. The larger number of collapse events in the stacked structures results in a higher average plateau stress level for a given relative density.

Out-of-Plane Loading

Single cores loaded in the out of plane configuration exhibit the same stress peak followed by an extended lower stress plateau as in-plane specimens, as shown in figure 2.9, but the serrations in the plateau are more regular and the stresses are significantly higher than for in-plane specimens. The out-of-plane configuration loads elements along their axis, so the compressive

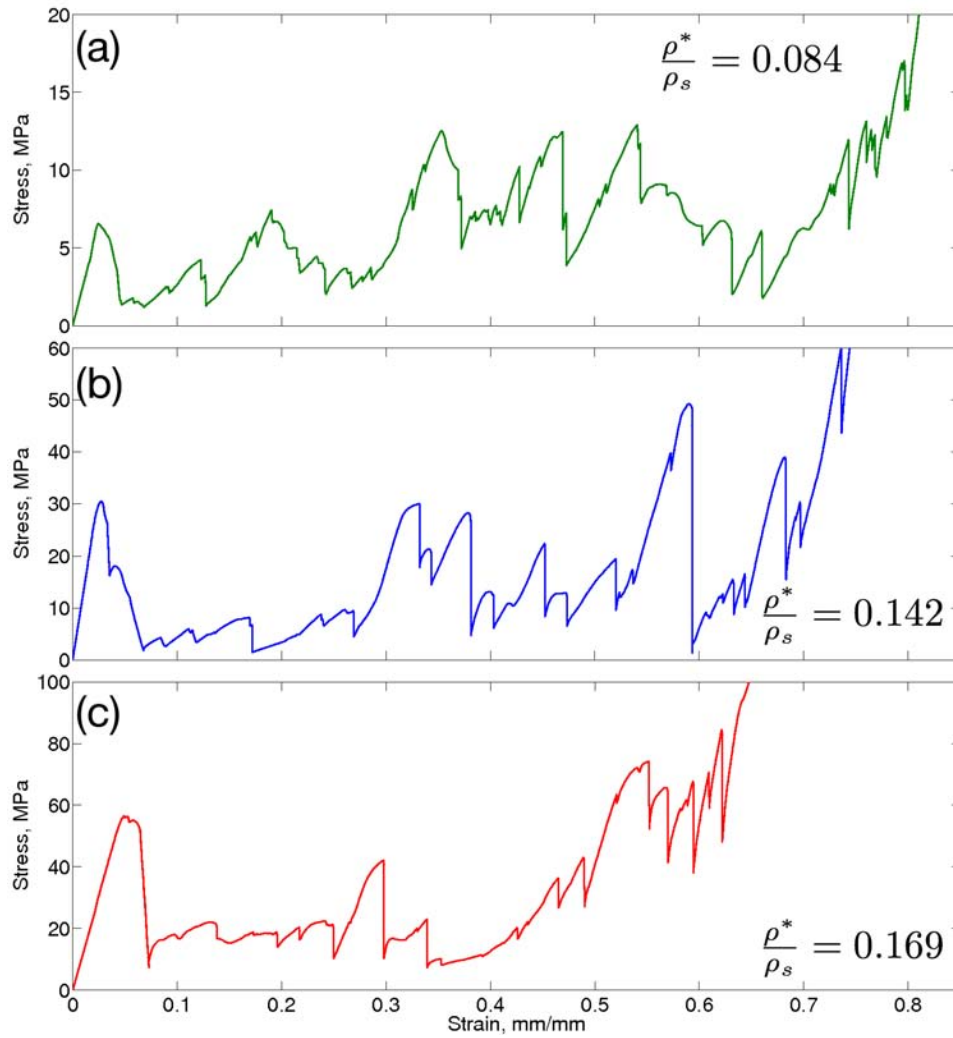


Figure 2.8: Stress-strain response of quasi-statically loaded multi-core stacks of corrugated metallic glass with relative densities of (a) 0.084, (b) 0.142, and (c) 0.169.

strength of the solid material is tested, as opposed to in-plane loading, where the strength of the structure comes from the bending strength of the struts. Figure 2.10(a), (b), and (c) show a single core at several strains during out-of-plane compression. A closer look at the core after the initial collapse event (figure 2.10(b)) shows that the fracture that occurs in these samples spans multiple struts and is oriented at an angle of roughly 45° to the axis of loading. These samples seem to fail as though they were thicker samples and not as though they were a collection of individually yielding struts, as with in-plane loading, one collapse event which affects multiple struts in a sample with a small number of elements causes a significant drop in a stress-strain curve. Despite these collapse events these cores maintain some structural integrity because of the alignment of the elements with the axis of loading, which results in smaller stress drops and a higher stress plateau. The data for a BMG single core are also compared to the stress-strain response of a stainless steel single core of the same relative density in Fig 2.9(b). The metallic glass core shows a significantly higher yield stress and plateau than the stainless steel specimen.

Discussion and Analysis

The relationship between relative strength and relative density for in-plane and out-of-plane metallic glass specimens is shown in figure 2.11(a). The fit lines to the in-plane data for single cores and stacks show exponents of essentially $n = 2$. This along with the microscopic evidence of permanent plastic deformation and multiple shear bands seen in figure 2.7 suggests that these in-plane structures do, indeed, yield plastically, and are, therefore, able to inherit the high yield strength of the parent metallic glass. The strengths of the out-of-plane structures are about 5–10 times higher than for the in-plane

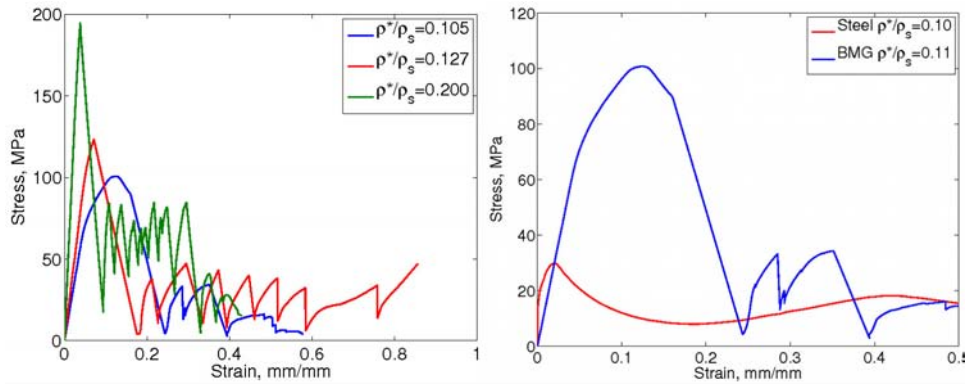


Figure 2.9: (a) Stress-strain response of three out-of-plane quasi-statically loaded metallic glass cores. (b) Comparison of stress-strain behavior of BMG core and Steel core of nearly the same relative density. Steel data from Côté et al. [47].

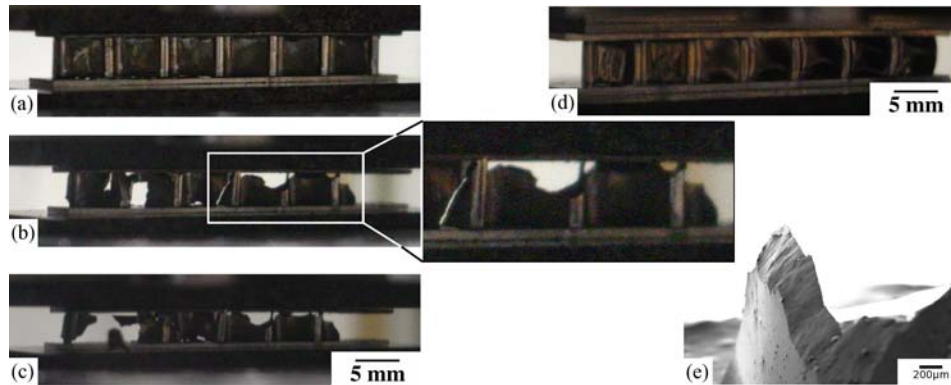


Figure 2.10: Images showing a metallic glass corrugation loaded in compression: (a) in the elastic region, (b) after the first collapse event showing failure that spans several struts at an angle of roughly 45° to the axis of loading, and (c) after several collapse events. (d) A corrugation with $\rho^*/\rho_s = 0.105$ whose struts were thin enough to buckle, and (e) a micrograph of a specimen after out-of-plane compression showing a failure along a single shear band.

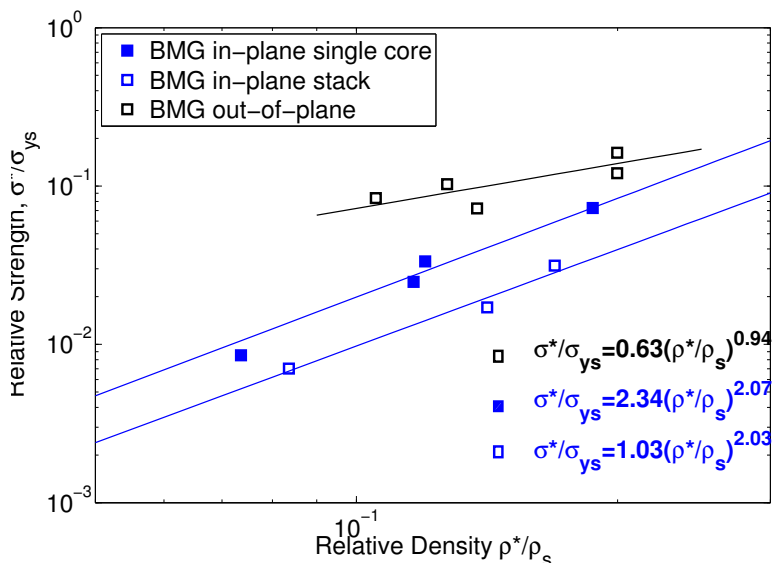


Figure 2.11: Relative strength-relative density plot for metallic glass structures tested in-plane and out-of-plane. Lines are power law best fits to the data.

structures, but the fit line to the out-of-plane data shows an exponent of $n = 0.94$, which is consistent with brittle failure. This assessment is supported by the observation of macroscopic brittle failure in figure 2.10(b) and the lack of shear bands around the fracture surface observed in figure 2.10(e). The corrugated specimen seems to behave more like a specimen that is larger than the plastic zone size of the alloy. As the struts are already well below the plastic zone size for low density structures, the only way to avoid brittle fracture of out-of-plane specimens could be to make the walls thin enough to buckle elastically.

When the strength of the in-plane metallic glass structures is compared to the strength of existing structures of the same geometry made of steel [46], as in figure 2.12(a), we see that the metallic glass specimens have strengths several times higher than the steel structures for the tested relative densities.

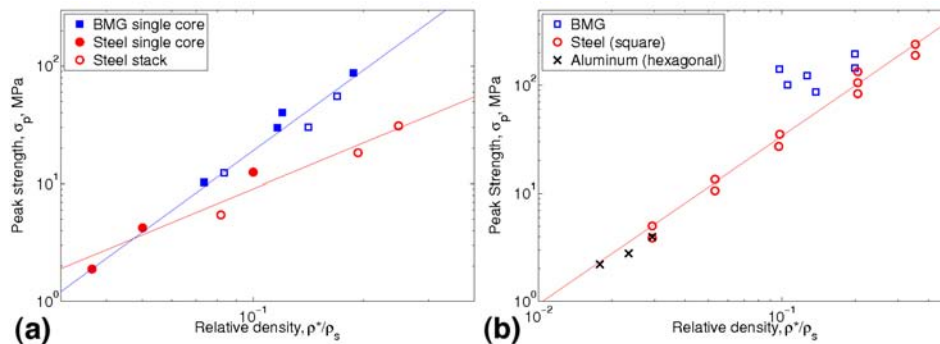


Figure 2.12: Strength-relative density relation for metallic glass and stainless steel cores (closed symbols) and stacks (open symbols) compressed (a) in-plane and (b) out-of-plane. Lines are power law best fits through the data. Steel data from ref. [46, 47].

The yielding mechanism for in-plane metallic glass structures has already been determined to be plastic yielding of the struts, so the greater strength can be attributed to the yield strength of the metallic glass being several times higher than the yield strength of the stainless steel.

The strength-porosity relationships for the out-of-plane metallic glass cores and square stainless steel honeycombs (from Côté et al. [47]) are shown in figure 2.12(b). Much like the in-plane specimens, the out-of-plane metallic glasses exhibit strengths several times higher than the square stainless steel structures. The metallic glass shows a lot of scatter in these strength values, so the fit to the data is not very good, but the data show a loose trend with a relatively low slope. As seen above, these structures have struts that act brittle, but are still very strong.

The energy absorption of the structures was measured by integrating the stress-strain curve from the yield point to the point where the curve increases beyond σ^* and does not drop below there again. This point corresponds roughly with the densification strain. The area is shown graphically for the

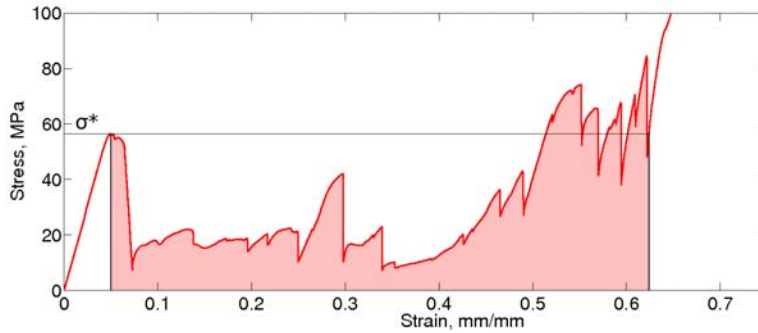


Figure 2.13: Stress-strain curve for a stack of metallic glass cores showing calculation of energy absorbed (shaded area).

stress-strain curve for a stack of metallic glass cores in figure 2.13 and has units of energy per unit volume. In most energy absorbing materials, low weight is desirable, so it is more useful to look at energy absorbed per unit mass. The energy absorption capabilities of the in-plane and out-of-plane structures are compared with those for stainless steel structures [46, 47] in figure 2.14. The metallic glass structures show energy absorption capabilities two orders of magnitude higher than those of the stainless steel structures for in-plane loading, and the data from stacks show higher energy absorption than the single cores. This is due to the larger number of struts in stacks which result in higher sustained stresses in the plateau region of the stress-strain curve. Despite the fact that the out-of-plane specimens appear to fail in a brittle manner, the energy absorption is 10–100 times higher than that for steel square honeycombs of the same density. This high energy absorption is the product of the high yield strength of the metallic glass and the ability of the low-density structure to allow struts to fail without catastrophically collapsing as a whole.

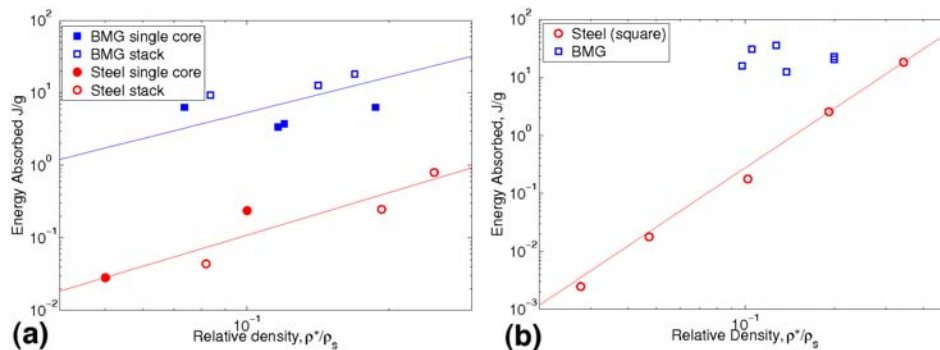


Figure 2.14: Energy absorption diagram for metallic glass cores and stacks and stainless steel structures in (a) in-plane and (b) out-of-plane loading. Lines are power law best fits through the data.

Conclusion

Periodic cellular amorphous metal structures were produced using thermo-plastic forming techniques and compressed in both in-plane and out-of-plane configurations. The in-plane specimens were shown to yield by plastic yielding of the individual struts and stacks containing larger numbers of struts were shown to exhibit higher sustained plateau stresses than single cores. Out-of-plane specimens were observed to fail in a brittle manner, but maintained high yield strengths and plateau stresses expected from the metallic glass. These materials also show greater strength and energy absorption capabilities than existing steel structures of similar geometries and relative densities. Specifically, energy absorption measured for metallic glass structures is observed to be higher by 10–100 times than that of steel structures.

Chapter 3

Metallic Glass Matrix Composite

Honeycombs

Introduction

Recent discoveries in metallic glass matrix composites have resulted in some of the toughest materials known [23, 48]. These materials are the result of the realization that certain glass-forming systems can be solidified with an interspersed soft dendrite phase resulting in enhanced mechanical properties [49], and that the dendrite is chemically stable in the presence of the liquid so that semi-solid processing is possible and results in a controlled microstructure [50]. This control of the microstructure allows for a composite to be made where the spacing between the dendrites is smaller than the plastic zone size of the metallic glass matrix which allows shear bands to form in the glass and be interrupted by the soft dendrites before fracture occurs causing more shear bands to form in the glass, and so on, resulting in global ductility and the high strengths expected from metallic glass. The resulting materials have extraordinary properties with strengths up to ~ 1.5 GPa and tensile ductility up to $\sim 10\%$ strain to failure [23]. Further studies of in situ composites have shown that specimens fabricated by semi-solid processing

followed by techniques such as hot forging [51], cold rolling, and thermo-plastic forming [52] maintain the extraordinary mechanical properties that are characteristic of these materials. These in situ composites are excellent candidates for use in cellular metals because of extraordinary mechanical properties, and the variety of available processing methods make it possible to fabricate interesting net shapes of the material.

As discussed in chapter 1, cellular metals have been studied extensively because of the interesting collection of properties including relatively high strength and stiffness at low densities and high energy absorption [24]. The properties of periodic cellular structures made from a bulk metallic glass were investigated in chapter 2, and were shown to exhibit strengths much higher and energy absorption capabilities nearly 100 times better than stainless steel honeycombs. Because these new metallic glass matrix composites have comparable strengths and ductility well beyond that seen in metallic glass, they should be excellent materials for use in cellular structures.

The design of a cellular structure made from these metallic glass matrix composites is similar to that for bulk metallic glass structures, but yielding by brittle fracture should not be a problem because the plastic zone size of the composites is on the order of millimeters [23]. Elastic buckling, however, could still be an issue, so the slenderness ratio of struts must be restricted. Following analysis carried out in chapter 2, the critical slenderness ratio, $(L/r)_{cr}$, is found to be between about 10 and 50 which is the same range as for BMG struts because the yield strain, $\varepsilon_y = E/\sigma_y$ is about 0.02 for both materials.

Methods

Corrugated sheets and egg-box structures of a metallic glass matrix composite alloy with composition $\text{Zr}_{36.6}\text{Ti}_{31.4}\text{Nb}_7\text{Cu}_{5.9}\text{Be}_{19.1}$ were fabricated by semi-solid induction forging under an argon atmosphere with water cooled copper dies as described in reference [51]. The dies for these sheets were designed to make an equilateral triangle honeycomb-type structure similar to the bulk metallic glass (BMG) cores of the previous chapter. Corrugated sheets with struts of thickness between 0.47 and 0.85 mm and resulting slenderness ratios of 10 or less and egg-box structures with relative densities as low as 11% were used in this study. The sheets were characterized using XRD to ensure that the amorphous and bcc phases were present in the as formed material, as shown in figure 3.1 (from [51]). The sheets were cut into rectangular strips, the compressed faces were ground plane parallel prior to testing. Single cores and two-core stacks were compressed quasi-statically in the in-plane configuration and single cores were compressed in the out-of-plane configurations with an applied strain rate of 10^{-3} s^{-1} . Compression experiments for the egg-box structures were also carried out at an applied strain rate of 10^{-3} s^{-1} . Tests were carried out with a screw-driven Instron universal testing machine with a load capacity of 50 kN and displacements were measured with a linear variable differential transformer. The cores tested here range from 0.25 to 0.35 in relative density and the egg-boxes have relative densities around 0.12. The relative densities of the specimens were calculated using the density of the solid as-forged material (as measured by Archimedes' method) and the measured volume of the rectangular prism occupied by the specimen.

These corrugated strips and egg-boxes were compressed with flat tool steel plates as the top and bottom sandwich layers. The metallic-glass-matrix-composite (MGMC) structures were not bonded to the tool steel plates. For the two-core stacks, several materials were tested as the middle plate (tool

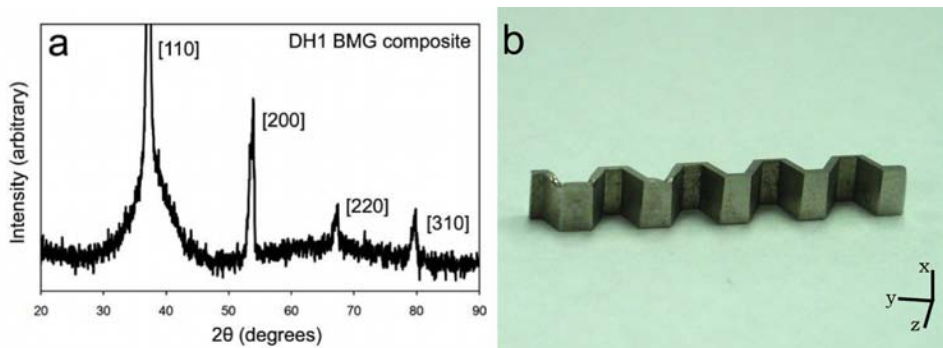


Figure 3.1: (a) XRD of as forged corrugation verifying phase character of the metallic glass matrix composite showing amorphous background and indexed bcc crystal peaks (from Hofmann et al. [23]). (b) Image of metallic glass matrix composite as prepared for quasi-static compression. The z-axis is the in-plane loading axis, and the x-axis is the out-of-plane loading axis.

steel, metallic glass matrix composite, and bulk metallic glass). The choice of mid plate did not, however, significantly alter the stress-strain behavior of the stacks. The data for two-core stacks presented here were gathered on specimens with a BMG or MGMC mid plate.

Results and Discussion

In-Plane Loading

The stress-strain response of quasi-statically loaded single cores and two-core stacks for in-plane and out-of plane loading is shown in figure 3.2. Images of a representative single core specimen during a compression test are shown in Fig 3.3(a) through (c). The single cores exhibit strains of 20% or greater before exhibiting a non-catastrophic collapse event, then load again and maintain a plateau of about half of the yield strength through to densification. Figure 3.3(b) shows that the primary failure event in an MGMC core is quite

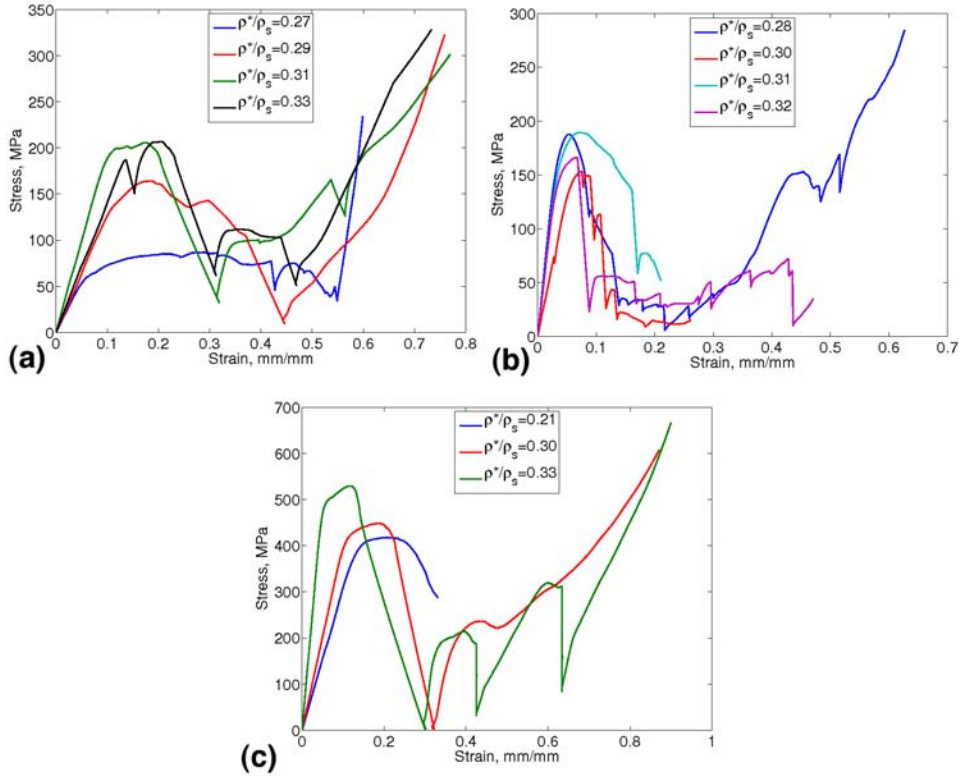


Figure 3.2: Stress-strain response of (a) single cores and (b) two-core stacks of MGMC corrugated sheets for quasi-static in-plane loading and (c) single cores in quasi-static out-of-plane loading.

localized and visually far less catastrophic than the similar image of metallic glass core in figure 2.7(c). Micrographs of compressed specimens seen in figure 3.3(d) and (e) also show macroscopic evidence of plastic deformation and a dense network of shear bands in the region of this deformation.

The two-core MGMC stacks show high yield stresses, but plateau stresses of only $\sim 25\%$ of the yield stresses (figure 3.2(b)). Photographs of a stack of MGMC cores during a compression test are shown in figure 3.4. The collapse of one strut results a significant rearrangement of the nearby nodes. In the example shown in figure 3.4(b) this has resulted in the misalignment

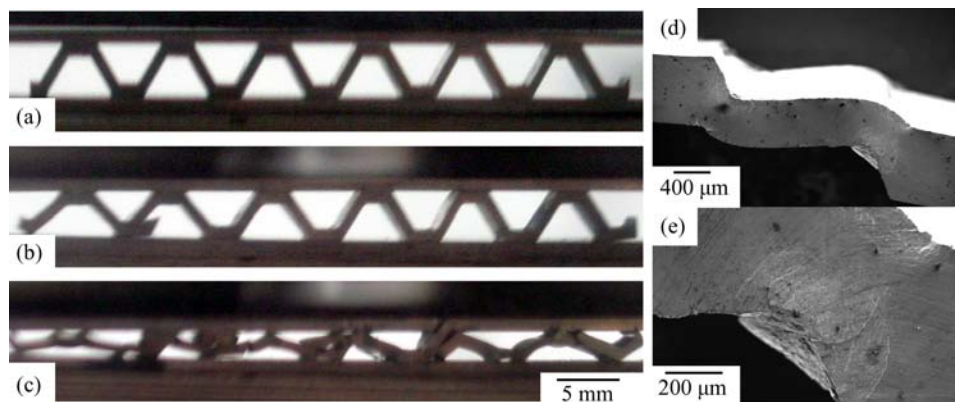


Figure 3.3: Images of a single core of the MGMC (a) in the elastic region, (b) after the first collapse event, and (c) near densification, and electron micrographs of a specimen after compression showing (d) severe plastic deformation and (e) a dense network of shear bands in the area of severe plastic deformation.

of several of the nodes. As the compression continues, the deformation is not uniform across the structure as nodes slide and rotate while the load is held by a small number of critical struts. Eventually the plateau stress rises, but only shortly before densification as seen in the stress-strain curve for the $\rho^*/\rho_s = 0.28$ specimen in figure 3.2(b).

The out-of-plane specimens show very high yield strengths and plateau stresses with stress dropping to very low values when collapse events occur (figure 3.2(c)). In the large plastic region just after yielding, these specimens show some buckling of cell walls prior to any collapse event. This buckling can be seen in figure 3.5(b). The initial collapse events in these in these samples result in a single huge shear band which cuts through the entire core as seen in figure 3.5(c). Further deformation in compression yields more large deformations along shear bands in the specimen, as seen in figure 3.5(d), in addition to more stable plastic deformation due to smaller shear bands

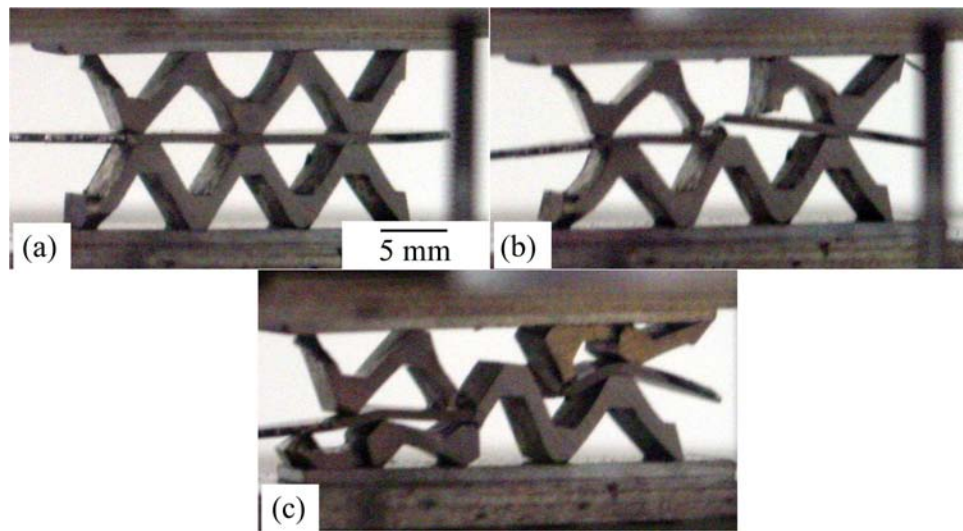


Figure 3.4: Images of a two-core stack of the MGMC (a) in the elastic region, (b) after the first collapse event showing that the nodes of the two cores are now misaligned, and (c) further deformation of the structure showing that the plastic deformation is not uniform across the structure.

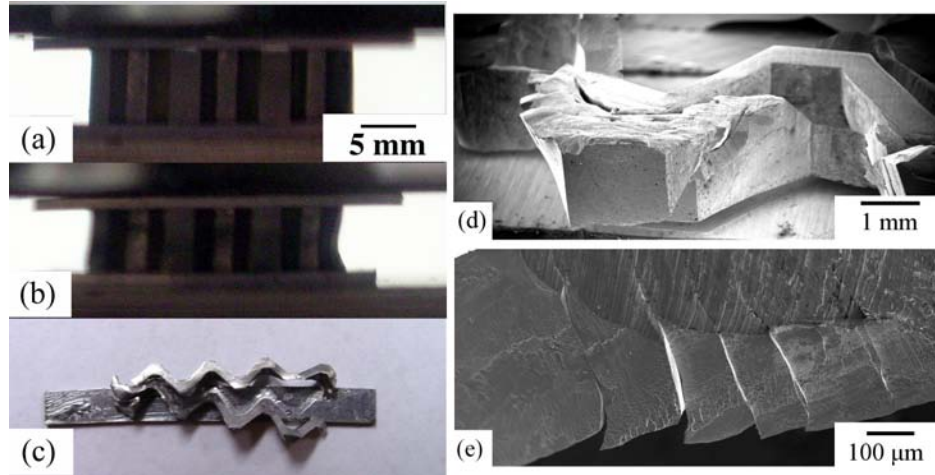


Figure 3.5: Images of out-of-plane MGMC specimens during testing (a) in the elastic region and (b) showing plastic buckling in the plateau after yielding and (c) top view after the first collapse event. Electron micrographs of an out-of-plane MGMC specimen: (d) side view showing massive deformation along large shear bands and (e) shear bands on top compression surface.

seen in figure 3.5(e) between collapse events. The collapse events in these specimens appear to have the same nature as the collapse events seen in the metallic glass cores in chapter 2 in the sense that when the dominant shear band travels through the specimen, it affects multiple struts and treats the corrugated sheet as a monolithic specimen, and not a collection of connected columns. The fact that the shear band affects the entire MGMC core and affects only several struts in the BMG cores is probably because the slenderness ratio of the typical strut, and therefore the relative density, of the MGMC cores is several times that of the BMG specimens, so the core loaded out-of-plane is effectively more like a thick column of uniform cross section.

The egg-box is a more porous structure, which using the same processing technique results in a lower density structure. The cell walls in the egg-box are also constrained along three edges as opposed to the corrugated sheets

where the cell walls have only two parallel constrained edges, so the structure is a bit more stable against buckling. As seen in figure 3.6(a) and (b), these structures are able to deform to full densification while remaining largely in one piece. The stress-strain response (figure 3.6(c)) shows a peak in stress much like the other MGMC structures, but the drop in load is not nearly as precipitous, and the plateau is relatively uniform in stress. The less severe drop in stress after the peak is attributed to the geometry of the structure as the cells fully span only the vertical dimension of the structure so when one cell wall fails, a smaller portion of the specimen is affected. In the case of the single core specimens, each cell spans both the height and the depth of the specimen, so when one strut breaks, it affects a large part of the structure. The stress drop could be further ameliorated by using specimens with even larger numbers of cells.

The relative strength-relative density relationships for MGMC corrugations are shown in figure 3.7. In-plane structures show an exponent of $n = 0.84$ that does not seem to correspond with any of the relative strength-relative density relations presented in ref. [24]. The data span only a small range of relative densities and show a bit of scatter, so the power law fit is not very good and the mechanism of failure cannot be determined by this method. As these materials are known to show ductility in tension [23], and the images in figures 3.3 and 3.4 show macroscopic and microscopic evidence of plastic deformation, the expected mechanism of yielding for an in-plane MGMC structure is plastic yielding of its struts.

The out-of-plane cores show strengths several times higher than in-plane structures with a fit exponent of $n = 1.58$ which, as discussed in chapter 2 corresponds to plastic buckling of cell walls in out-of-plane loading. These data also span only a small range of relative densities, but they show a clear trend and the power law fits them well. This buckling can be seen in

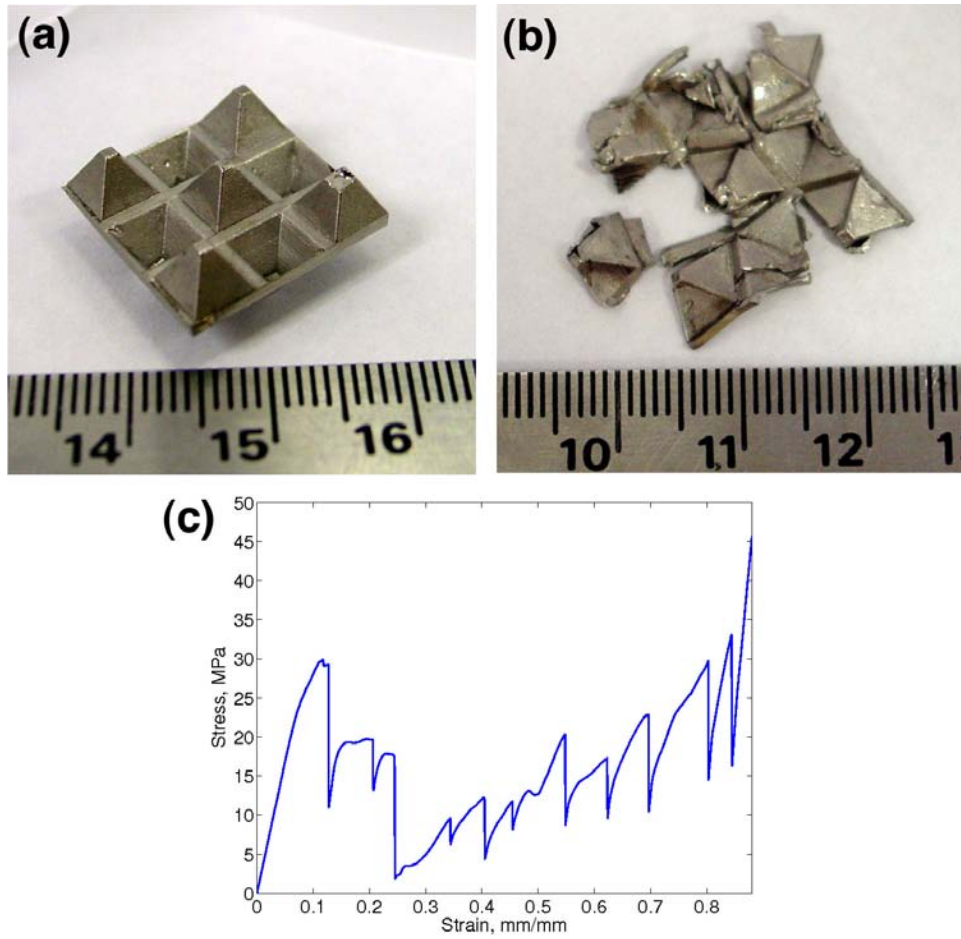


Figure 3.6: Images of an MGMC egg-box structure (a) as prepared for testing and (b) after testing showing the ability to flatten almost completely and remain largely in one piece. (c) Stress-strain response of a representative egg-box with $\rho^*/\rho_s = 0.12$.

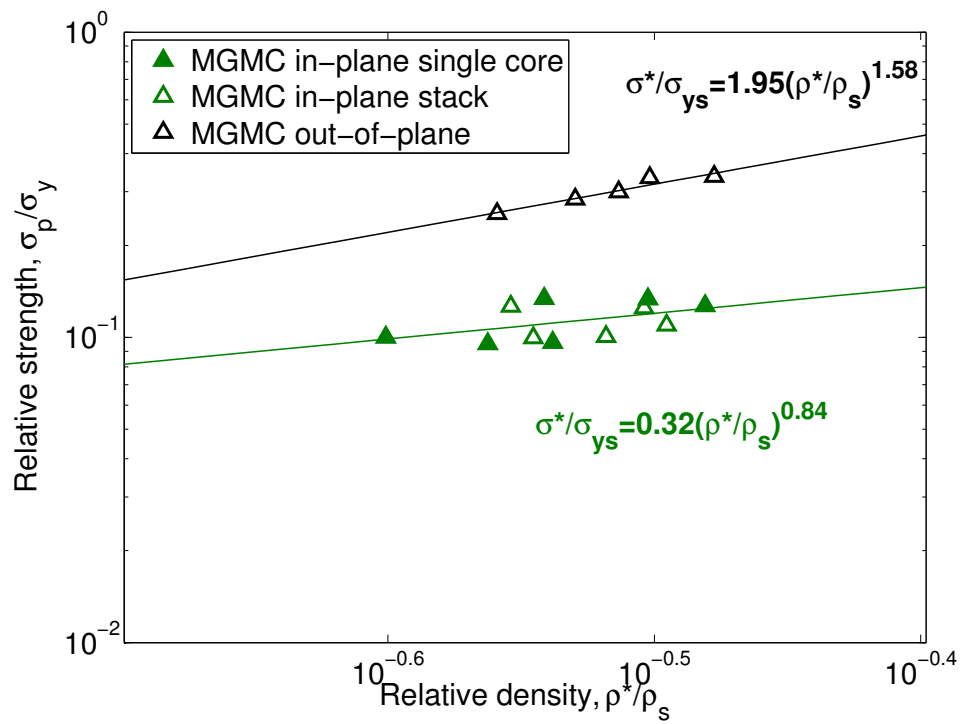


Figure 3.7: Relative strength-relative density plot for MGMC structures in in-plane and out-of-plane loading. Lines are power law best fits to the data.

figure 3.5(b), and micrographic evidence of the plastic nature of the yielding in the form of shear bands can be seen in figure 3.5(d) and (e), so the out-of-plane MGMC cores definitely yield plastically.

When these structures are compared to the data for existing structures made from stainless steel, as in figure 3.8, the MGMC shows strengths 4–5 times higher than for steel structures of nearly the same relative density with very high sustained plateau stress. The curve for the out-of-plane MGMC in figure 3.8(b) shows a total strain of about 35% as opposed to almost 80% for the steel because this test was carried out only until the first collapse event and not to densification. The stress-strain response of the 12% dense egg-box structure is higher in stress in almost every respect to an 8% dense stainless steel honeycomb and shows significantly higher peak stress and roughly equal sustained plateau stress when compared to a stainless steel honeycomb with 19% relative density, as seen in figure 3.8(c).

Comparing MGMC structures with those made from crystalline metals and the BMG structures over a range of relative densities, we can see that the peak strength of MGMC structures falls generally in line with the peak strength of the BMG structure for both in-plane and out-of-plane loading, which is significantly higher than the strength exhibited by stainless steel structures in in-plane and stainless steel and aluminum structures in out-of-plane loading over a range of relative densities (figure 3.9). The egg-box structures are plotted with the in-plane structures as their cell walls are also loaded in a bending mode and not in compression like for out-of-plane loaded honeycombs. The higher strength of the metallic glass and composite structures is the result of the higher strength of metallic glass and composite parent materials.

Energy absorption of the MGMC structures was calculated in the same manner as the for BMG structures in chapter 2. The energy absorption

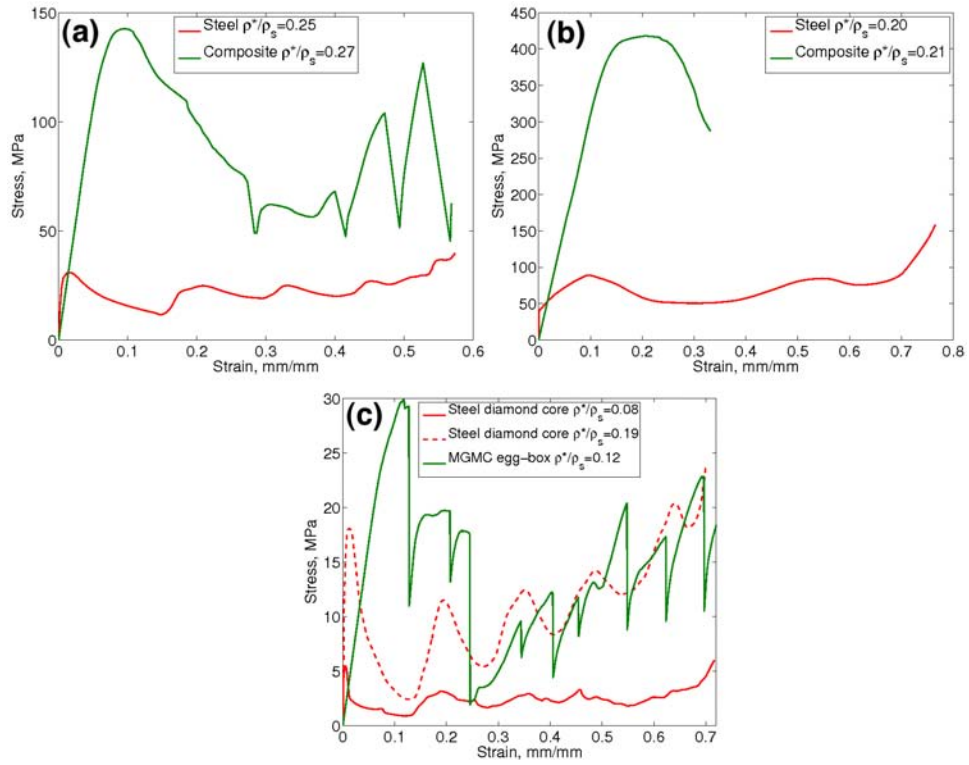


Figure 3.8: Stress-strain plots comparing the behavior of MGMC structures with steel structures of roughly the same density and similar geometry for (a) in-plane honeycomb, (b) out-of-plane honeycomb, and (c) egg-box structures. Steel data from refs. [46, 47]

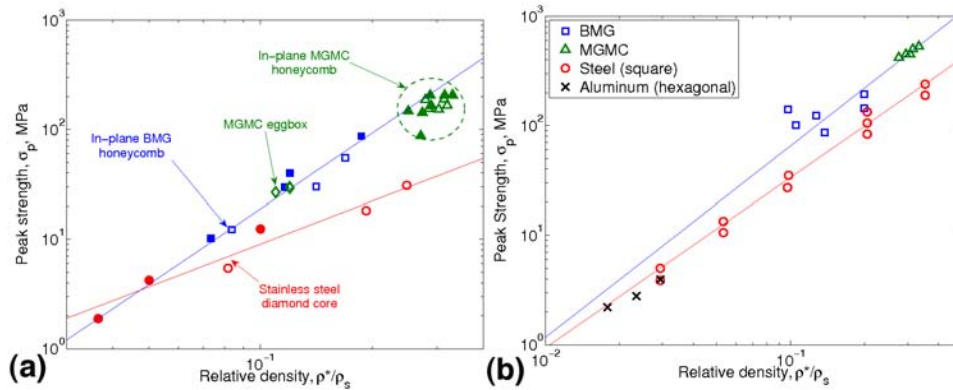


Figure 3.9: Strength-relative density plots for BMG and MGMC structures and crystalline metal structures under (a) in-plane and (b) out-of-plane loading. Steel and aluminum data from refs. [46, 47]

capabilities of the MGMC structures are shown in figure 3.10. The composite structures are capable of absorbing between three and five times more energy than structures made of crystalline metals for both honeycomb loading configurations. Again, the egg-box structures are plotted along side the in-plane honeycombs, and they show at least a fivefold increase in energy absorption over steel honeycombs of the same relative density. This high energy absorption is the consequence of the high strength of the metallic glass matrix composite material, and the ability of the structure to collapse non-catastrophically allowing it to maintain a high plateau stress throughout densification.

The plateau stress is quite an important property in the selection of an energy absorbing structure, as it determines the stress that is transmitted through the structure to whatever it is that the structure is trying to protect. figure 3.11 shows the energy absorbed per gram of structure in relation to the plateau stress. For a selected plateau stress, the MGMC structures absorb 4 to 5 times as much energy per gram of structure than the stain-

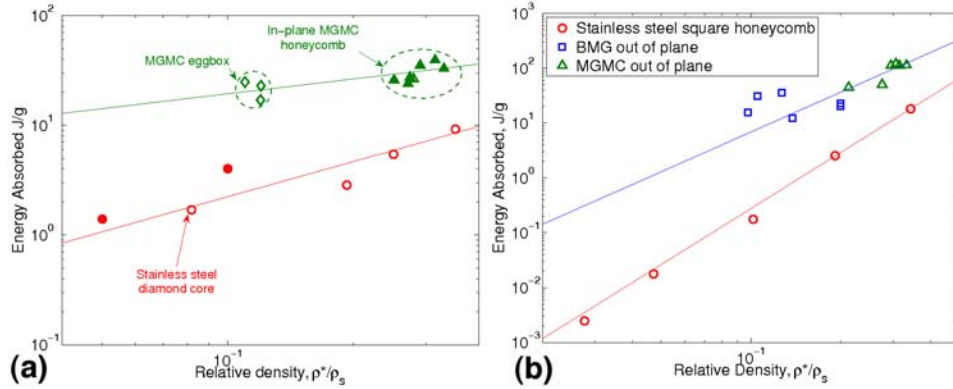


Figure 3.10: Energy absorbed per unit mass versus relative density plots for BMG and MGMC structures and crystalline metal structures under (a) in-plane and (b) out-of-plane loading. Steel data from refs. [46, 47]

less steel honeycombs. From the perspective of this materials selection plot, the MGMC structures beat the steel structures because the MGMC parent material has much higher yield strength than stainless steel and it is also significantly lighter (5.68 g/cm^3 for $\text{Zr}_{36.6}\text{Ti}_{31.4}\text{Nb}_7\text{Cu}_{5.9}\text{Be}_{19.1}$ compared to 8.00 g/cm^3 for the 304 stainless steel used in the structures from Côté et al. [46, 47]).

Conclusion

Periodic structures have been produced from in situ metallic glass matrix composites using a semi-solid induction forging technique, and their mechanical properties examined for both in-plane and out-of-plane configurations. Egg-box structures have also been produced from the MGMC and tested. These structures have relative densities ranging from $\rho^*/\rho_s = 0.11$ to $\rho^*/\rho_s = 0.35$. Because of the narrow range of relative densities for the honeycombs ($\rho^*/\rho_s = 0.25$ to 0.35), it is difficult to glean the yielding mechanism

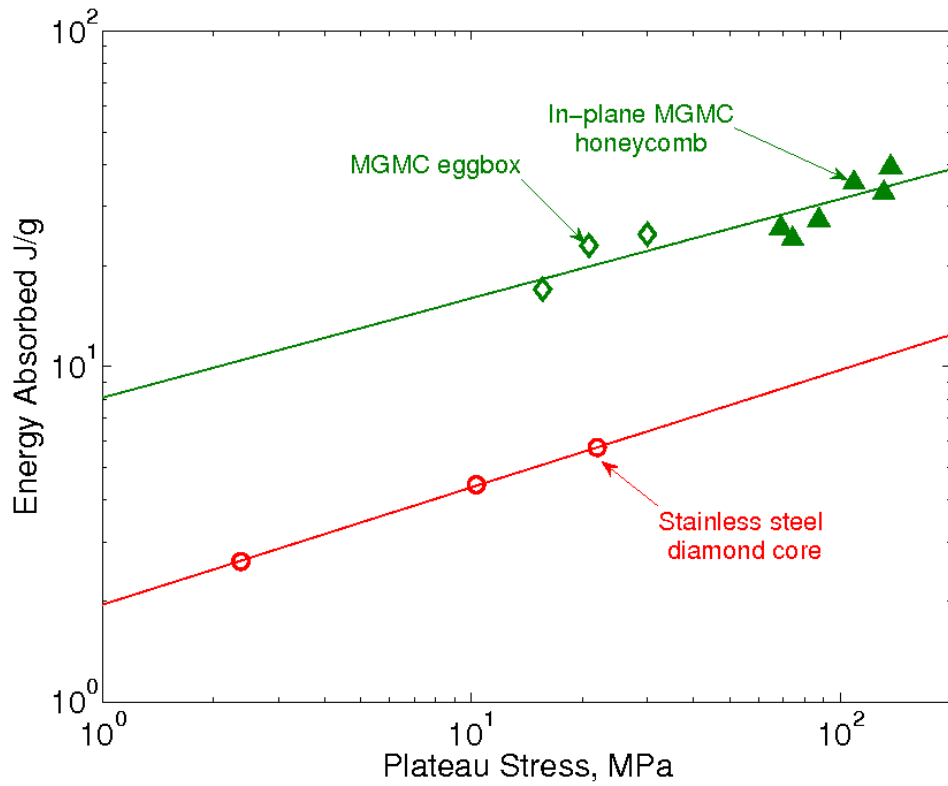


Figure 3.11: Energy absorbed per unit mass versus plateau stress for MGMC structures and crystalline metal structures showing very high energy absorption capabilities of MGMC structures. Steel data from ref. [46].

from the relative strength–relative density relationship, but the material is ductile, micrographs show evidence of plastic deformation, and the struts are far too thick to buckle elastically, so the yielding mechanism of these structures is believed to be plastic yielding. The metallic glass matrix composite structures show strengths that are several times stronger than steel structures of the same relative density in both in-plane and out-of-plane loading. The energy absorption capabilities of these materials are just as impressive as those for metallic glass structures absorbing from several times to almost 10 times more energy than steel structures of the same relative density with stress plateaus that are more uniform than those of the metallic glass structures, but it is believed that they could be even better with further optimization of the structural geometry. Egg-box structures show slightly larger gains in strength and energy absorption over steel structures than do the honeycombs. These structures are lightweight and very strong with very high capacity for energy absorption.

Chapter 4

High Porosity Metallic Glass Foam: A Powder Metallurgy Route

Abstract

A powder metallurgy route to the fabrication of metallic glass foam is introduced. The method involves consolidating metallic glass powder blended with blowing agent particulates to produce expandable precursors, capable of yielding foams with porosities as high as 86%. The foams are found to inherit the strength of the parent metallic glass, and to be able to deform heavily toward full densification absorbing high amounts of energy ($>30 \text{ MJ/m}^3$).

The content of this chapter was previously published in Applied Physics Letters 2007;91(16).

Introduction

The ability of amorphous metals to soften and flow upon relaxation at the glass transition gives rise to a viscoplastic flow behavior that enables unique forming capabilities, similar to those of plastics and conventional glasses [53, 54, 55]. The development of highly porous metallic glass foam via viscoplas-

tic expansion of impregnated pores has recently emerged as an attractive thermoplastic forming process [28, 39, 56, 57]. In this chapter we demonstrate that by utilizing a powder metallurgy route, an efficient foaming process is made possible by which highly porous metallic glass foam can be fabricated. The advantages of using powder metallurgy to fabricate near-net-shape metallic glass components are well documented [38, 58]. By taking advantage of the viscoplastic flow characteristics of the supercooled liquid state, highly consolidated metallic glass components have been produced having dimensions that exceed the critical casting thickness of the monolithic glass while exhibiting the thermodynamic and mechanical properties of the glass. Moreover, composite [59] or porous [43] (<40% porosity) metallic glasses have been developed by mixing metallic glass powder with fugitive acid-soluble particulates. Here we show that by mixing metallic glass powder with blowing agent particulates, expandable precursors can be fabricated capable of yielding metallic glass foams with porosities as high as 86%, able to effectively inherit the strength of the glass and to deform heavily absorbing high amounts of energy.

Methods

The method introduced here involves consolidating the powder mixture at a temperature within the supercooled liquid region of the alloy but below the decomposition point of the blowing agent to produce a foam precursor. The precursor can be subsequently expanded into foam at a temperature within the supercooled liquid region and above the decomposition point of the agent. An ideal blowing agent for the present method should therefore chemically decompose to release gas at a temperature within the supercooled liquid region of the alloy, preferably closer to the glass transition temperature, T_g .

To ensure that the precursor and the foam remain amorphous, the durations for the consolidation and expansion processes should not exceed the time for the supercooled liquid to crystallize at the respective process temperatures.

In the present study we utilize a $\text{Pd}_{43}\text{Ni}_{10}\text{Cu}_{27}\text{P}_{20}$ glass. The glass transition and crystallization temperatures of this alloy are approximately 300°C and 400°C , respectively. The alloy was prepared by first prealloying Pd (99.9% purity), Ni (99.9% purity), and Cu (99.99% purity) by induction melting, and then alloying P (99.9999% purity) by step-wise furnace heating. The alloy ingot was fluxed with B_2O_3 at 720°C , and was subsequently water quenched to the amorphous state. The glassy ingot was crushed into a fine powder and was sieved into 0.425 mm mesh. The thermal analysis scan revealing the amorphous nature of the powder is presented in figure 4.1. As a blowing agent, magnesium carbonate, n-hydrate ($\text{MgCO}_3 \cdot n\text{H}_2\text{O}$) powder from J. T. Baker was employed. Thermogravimetric analysis of this powder revealed a slight mass loss accompanied by a weak endothermic reaction at $\sim 180^\circ\text{C}$, which can be associated with the release of H_2O vapor, followed by a severe mass loss accompanied by a strong endothermic reaction at $\sim 335^\circ\text{C}$, which can be associated with the decomposition of MgCO_3 releasing CO_2 . The massive release of CO_2 at a temperature slightly above T_g suggests that by properly consolidating the powder mixture at a temperature near T_g , an enormous amount of propellant gas can be available for viscoplastic foaming within the supercooled liquid region. The slight release of H_2O vapor at 180°C is found to have a negligible effect on the consolidation process.

A uniform powder mixture with minimal segregation consisting of 95 vol% $\text{Pd}_{43}\text{Ni}_{10}\text{Cu}_{27}\text{P}_{20}$ and 5 vol% MgCO_3 was prepared. Hot isostatic pressing (HIP) was performed to consolidate the mixture (American Isostatic Presses, AIP6-30H). A stainless steel canister (19.05 mm in diameter and 65 mm in length) containing the powder mixture was first evacuated and then e-beam

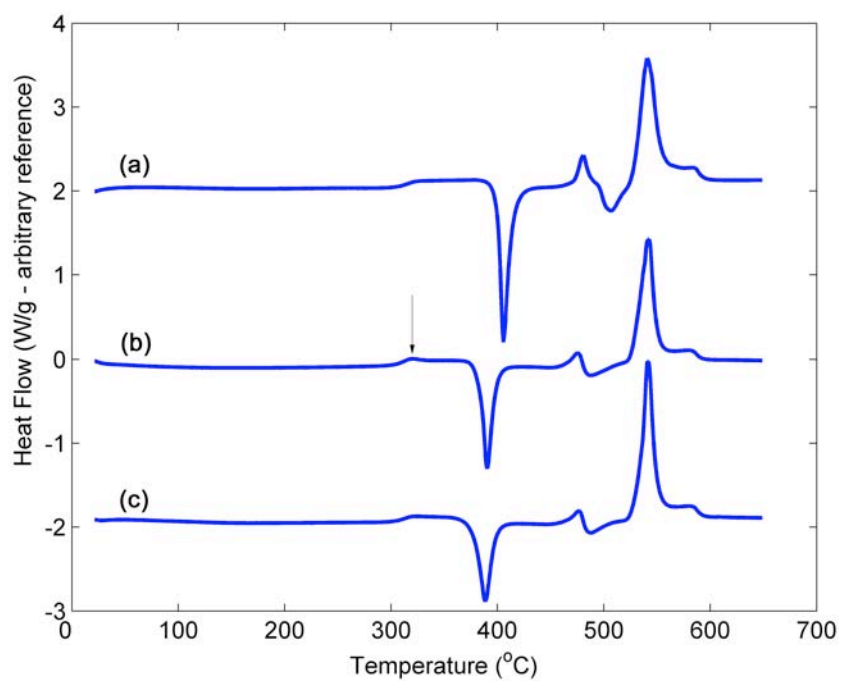


Figure 4.1: Differential calorimetry scans of the metallic glass powder (a), the precursor (b), and the foam (c). Arrow in (b) indicates a minor bump associated with the endothermic decomposition reaction of the agent.

welded. The HIP procedure consisted of applying a pressure of 207 MPa followed by a gradual temperature rise to $290 \pm 10^\circ\text{C}$. The mixture was held at the process temperature under the applied pressure for 2 hours. The density of the consolidated precursor (measured by the Archimedes method) was found to be the same as the monolithic solid to within measurement error ($9.34 \pm 0.01 \text{ g/cm}^3$). The thermal analysis scan revealing the amorphous nature of the precursor is presented in figure 4.1. The glass transition temperature of the consolidated precursor appears unchanged in reference to the glassy powder. However the crystallization temperature appears somewhat lower, possibly due to the presence of decomposed MgO acting as heterogeneous nucleant. It is interesting to note that a minor bump is observed slightly above T_g , which is consistent with the endothermic decomposition reaction of the agent.

Expansion of the consolidated precursor into foam was performed by inductively heating the precursor to a temperature within the supercooled liquid region under vacuum, holding for a period shorter than the time required for crystallization at that temperature, and subsequently quenching. Porosity was controlled by the temperature and duration of foaming. Various segments of the precursor were expanded at temperatures ranging between 340°C and 370°C for durations ranging between 10 and 100 s, accomplishing porosities that range between 4% and 86% (measured by the Archimedes method). An 82% porosity foam expanded at 350°C for 60 s is shown in figure 4.2. A precursor segment of equivalent mass is also presented alongside the foam in order to demonstrate the fivefold increase in volume produced by foaming. The fully glassy nature of the foam is verified by x-ray diffraction, shown in the inset of figure 4.2. The thermal analysis scan revealing the thermodynamic characteristics of the foam is presented in figure 4.1. Like the precursor, the foam exhibits a glass transition temperature consistent

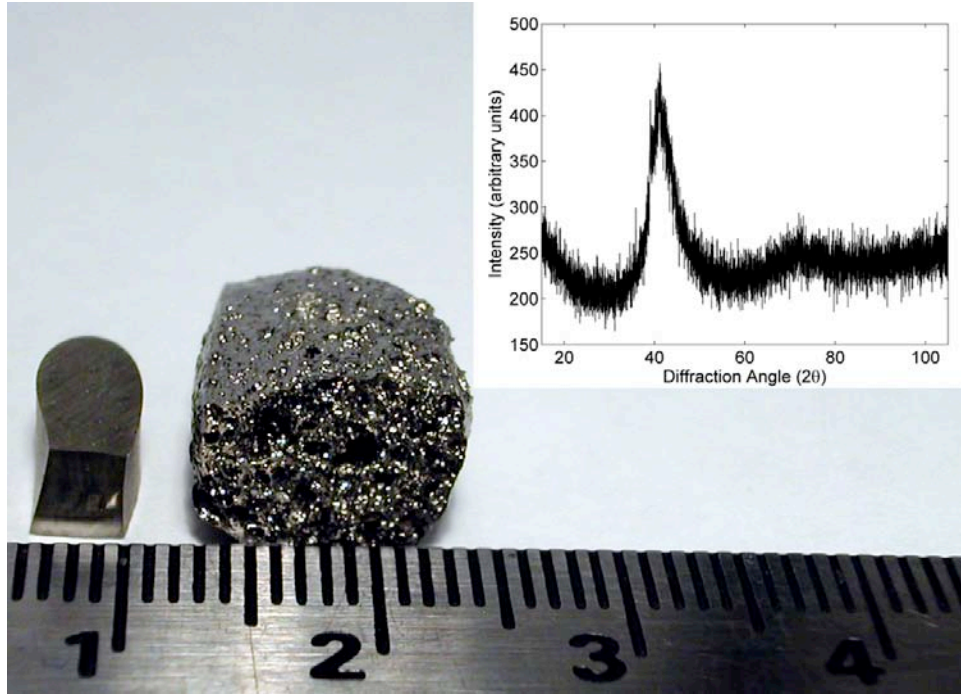


Figure 4.2: Image of an 82% porosity foam produced via the introduced powder metallurgy route, alongside a precursor segment of equivalent mass. Inset: X-ray diffractogram verifying the amorphous nature of the foam.

with the reference powder but a crystallization temperature that is slightly lower.

Results and Discussion

The microstructure of the consolidated precursor and the cellular structure of the 82% porosity foam were examined using scanning electron microscopy. A magnified view of a radial cross section of the precursor is shown in the micrograph of figure 4.3(a). The grooves between metallic-glass particulates are thin, and filled with blowing agent powder. The micrograph of figure 4.3(b) shows a highly magnified view of an interparticulate groove filled with blow-

ing agent powder. The chemical composition of the agent particulate agglomerates was verified by energy dispersive x-ray analysis. A magnified view of a radial cross section of the foam is shown in the micrograph of figure 4.3(c). A distribution of pore sizes is observed with a mean pore size on the order of 300–400 μm . Small amounts of blowing agent agglomerates can be detected within smaller pores, indicating that a small fraction of the blowing agent failed to fully decompose during expansion. Closer inspection in the vicinity of the solid region of the foam, presented in the micrograph of figure 4.3(d), reveals that the bonding between particles has improved considerably following foaming, an effect that can be attributed to the viscoplastic shear flow realized upon expansion. Consolidated struts with good particulate bonding can be expected to exhibit a strength close to the strength of the metallic glass, giving rise to a global foam strength consistent with the strength of the parent solid.

Compressive testing of foams with porosities of 4%, 40%, and 86% was performed. Square specimens with adequate homogeneity and sufficient number of cells per side having aspect ratios ranging between 1.2 and 1.5 were prepared. Strain rates of $1 \times 10^{-4} \text{ s}^{-1}$ were applied. Strains were measured using a linear variable differential transformer. The compressive stress-strain responses are shown in figure 4.4. The 4% porosity foam is shown to yield at a relatively high stress (650 MPa), however is able to undergo only minimal plastic deformation before failing catastrophically by an incipient collapse event. The 40% porosity foam fails at a lower stress (225 MPa), however since the principal collapse is non-catastrophic, the foam is able to undergo considerable plastic deformation at a plateau stress that is approximately 50% of the yield stress. It is interesting to note that the failure characteristics of the present 40% porosity foam are similar to the 40% porosity foam reported in ref. [43], which likewise fails by an incipient non-catastrophic collapse event

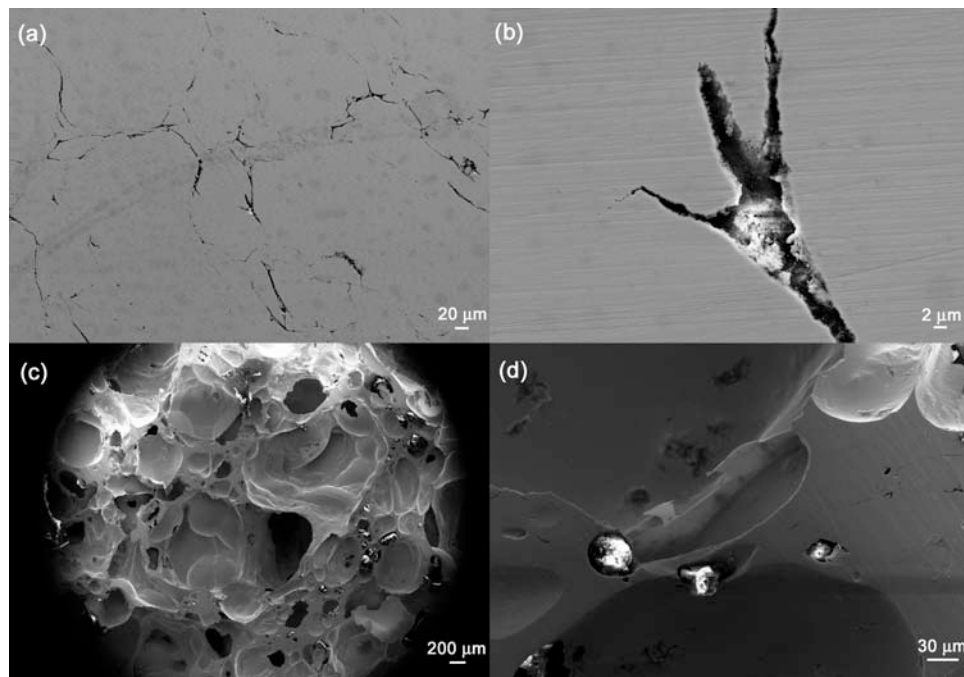


Figure 4.3: Scanning electron micrographs showing the microstructure of the precursor (a) and (b), and the cellular structure of an 82% foam (c) and (d).

characterized by a stress drop in excess of 30%. In contrast, the 86% porosity foam produced here yields at a considerably lower stress (25 MPa), however is capable of maintaining a plateau stress that is on average comparable to the failure stress. Consequently, as shown in figure 4.5, the 86% porosity foam is able to undergo plastic deformation to 80% strain. The densification strain of a foam ε_D , which together with the plateau stress dictate the foam energy absorption capability, is determined solely from the relative density ρ^*/ρ_s (in the limit of low ρ^*/ρ_s) according to $\varepsilon_D = 1 - 1.4(\rho^*/\rho_s)$ [24].

Thus, the densification strain for an 86% porosity foam can be estimated to be $\sim 80\%$, revealing that the present 86% porosity foam is capable of being deformed to ε_D . Due to a relatively high and, on average, constant plateau stress, the foam is thus able to absorb a considerable amount of mechanical energy prior to being fully densified. The specific energy absorbed by this foam can be estimated from the area under the stress-strain curve to be 31 MJ/m³. This value is nearly twice the value reported for another 86% porosity metallic glass foam [34]. The higher energy absorption capability of the present foam is attributed to its ability to maintain a relatively high plateau stress, which on average is higher than that of ref. [34] by nearly a factor of 2 (even though the parent metallic glass of ref. [34] is 10% stronger).

As discussed above, because of a well-consolidated strut microstructure, foam strengths that are consistent with the strength of the parent solid can be expected. Hence, we will attempt to correlate the foam failure stresses to the plastic yield strength of the glass. In the inset of figure 4.4, the foam failure stresses σ_y normalized by the solid plastic yield strength σ_{ys} (known to be 1630 MPa for Pd₄₃Ni₁₀Cu₂₇P₂₀ [29]) are plotted against ρ/ρ_s . The power law correlation for plastically yielding foams, given by $\sigma_y/\sigma_{ys} = 0.3(\rho/\rho_s)^{3/2}$ [24], is also plotted. The data for the 40% and 86% porosity foams appear to conform remarkably well to the established correlation, indicating that the

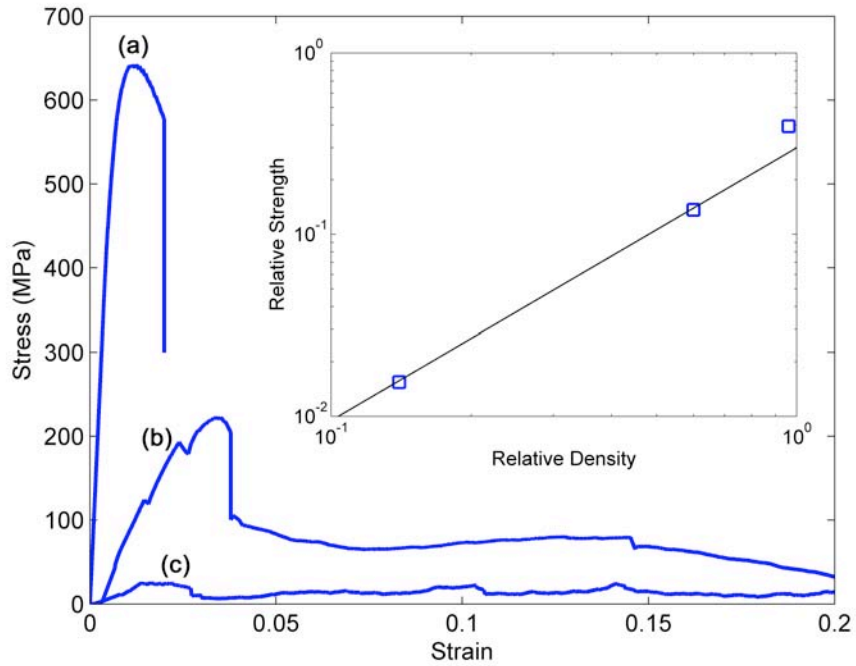


Figure 4.4: Compressive stress-strain diagrams of 4% (a), 40% (b), and 86% (c) porosity foams. Inset: Foam relative strengths plotted against relative densities. The solid line is a plot of the power law correlation established for plastically yielding foams [24].

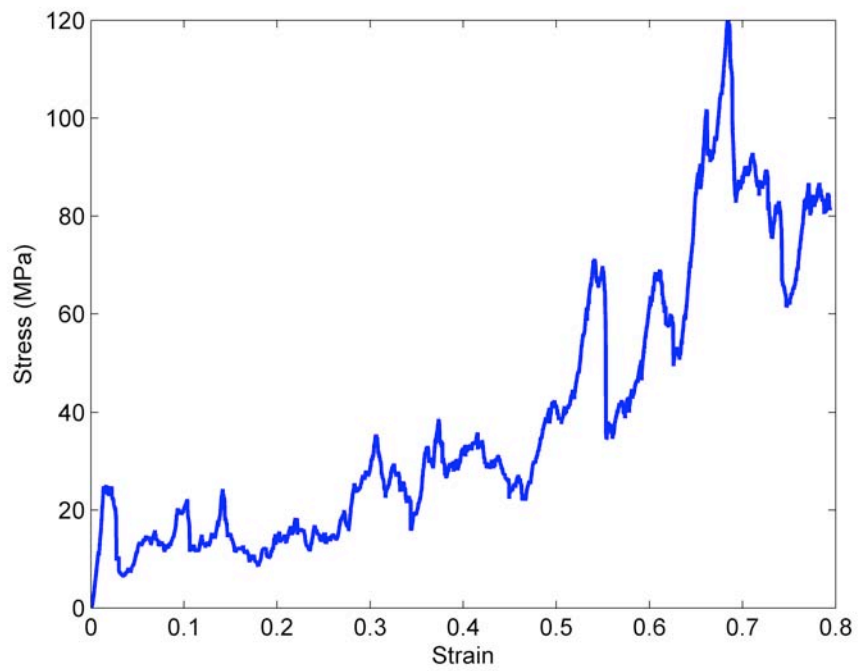


Figure 4.5: Compressive stress-strain diagram of an 86% porosity foam deformed toward full densification.

strengths of these foams scale consistently with the plastic yield strength of the parent glass. The slight deviation of the 4% porosity foam is attributed to the expected breakdown of the correlation at high relative densities [24]. It is also interesting to note that the Youngs moduli of these foams, which are estimated from the initial linear loading responses to be 95.7 GPa, 10.3 GPa, and 1.41 GPa for porosities 4%, 40%, and 86% respectively, scale reasonably with the solid Youngs modulus (reported to be 102 GPa [29]).

Conclusions

In summary, a powder metallurgy route to the fabrication of metallic glass foam was introduced. It was demonstrated that by consolidating metallic glass powder blended with blowing agent particulates, expandable metallic glass precursors could be produced which were capable of plastically yielding foams with porosities as high as 86%. The foams effectively inherit the high strength of the parent metallic glass, and are able to deform heavily towards full densification absorbing high amounts of energy.

Authors would like to acknowledge valuable discussions with J. Schroers and to express their gratitude to G. Garret and M. M. Palos for the valuable assistance.

Chapter 5

The Effect of Strain Rate on the Yielding Mechanism of Amorphous Metal Foams

Abstract

Highly stochastic amorphous $\text{Pd}_{43}\text{Ni}_{10}\text{Cu}_{27}\text{P}_{20}$ foams were tested in quasi-static and dynamic loading. The strength/porosity relations show distinct slopes for the two loading conditions, suggesting a strain-rate-induced change in the foam yielding mechanism. The strength/porosity correlation of the dynamic test data along with microscopy assessments support that dynamic foam yielding is dominated by plasticity rather than elastic buckling, which was previously identified as the mechanism governing the quasi-static yielding of these foams. The strain-rate-induced shift in the foam yielding mechanism is attributed to the convergence of the characteristic time for dynamic loading and the timescale associated with sound wave propagation across intracellular membranes, thereby suppressing elastic buckling and promoting plastic yielding.

The content of this chapter was previously published in Applied Physics

Letters 2010;96(2).

Introduction

Recent progress in the processing of metallic glasses has led to the development of open-and closed-cell amorphous metal foams fabricated from various alloys via a variety of methods [42, 43, 56, 60, 61, 62]. Because of the unique mechanical properties of amorphous metals, such as high strength and elasticity, broadly varying toughness, and lack of ductility [12], amorphous metal foams have been shown to inherit a collection of mechanical properties from the parent material not previously seen in porous solids of any kind. Specifically, cellular structures consisting of struts thinner than the process zone size of the amorphous metal were found to be heavily deformable, as catastrophic failure due to global brittle fracture is effectively avoided [30, 34]. On the other hand, highly stochastic cellular structures consisting of struts with broadly varying thicknesses and aspect ratios were found to yield by percolation of elastic buckling instabilities, a consequence of the high elastic limit of the amorphous metal [35]. The elastic yielding behavior of such highly stochastic foams gives rise to a steep strength/porosity relation, resulting in very high strengths and significantly more plasticity than monolithic (pore-free) materials at high relative densities [29], however as the limit of cooperative buckling is approached at low relative densities, the attainable foam strengths are substantially lower. By matching the structural scales controlling brittle fracture and buckling percolation, that is, by attaining cellular structures consisting of thin struts with uniform slenderness ratios, the foams can yield plastically at rather low relative densities (<10%) [36]. Consequently, such foams are able to inherit the high plastic yield strength of the amorphous metal at very high porosities, and thereby emerge among

the strongest foams of any kind.

The mechanical behavior of monolithic amorphous metals is known to be insensitive to strain rate [13, 63], but the strain-rate sensitivity of these porous solids has not yet been investigated. In this chapter, it is shown that unlike the parent solid, the yielding mechanism of a stochastic amorphous-metal cellular structure is sensitive to the rate of the applied strain, and consequently the slope of the overall strength/porosity relation for the foam material shifts with a drastic increase in the strain rate.

Methods

Amorphous $\text{Pd}_{43}\text{Ni}_{10}\text{Cu}_{27}\text{P}_{20}$ foam specimens with highly stochastic closed-cell porosity were utilized in this work. The foams were produced by thermoplastically expanding entrained bubbles in the supercooled liquid region, as described in Ref. [39]. The statistical distribution of pore sizes in such foams is analyzed in Ref. [57]. Dynamic and quasi-static compression tests were carried out on plane-parallel cylindrical specimens with relative densities ranging from 13% to 65%. For the dynamic tests, specimens with heights of about 6 mm were used. A representative dynamic-test specimen is shown in figure 5.1(a). For the quasi-static tests, specimens with aspect ratios around 1.0 were used. Porosities of all samples were measured using the Archimedes method.

For the quasi-static tests, a screw-driven Instron universal testing machine with a load capacity of 50 kN was used. Displacements were measured using a linear variable differential transformer. Strain rates for the quasi-static tests ranged between 10^{-3} and 10^{-4} s^{-1} . The dynamic compression experiments were carried out on a 19.05 mm diameter split Hopkinson (Kolsky) pressure bar made of C300 Maraging steel at strain rates between 3000 and 3500 s^{-1} .

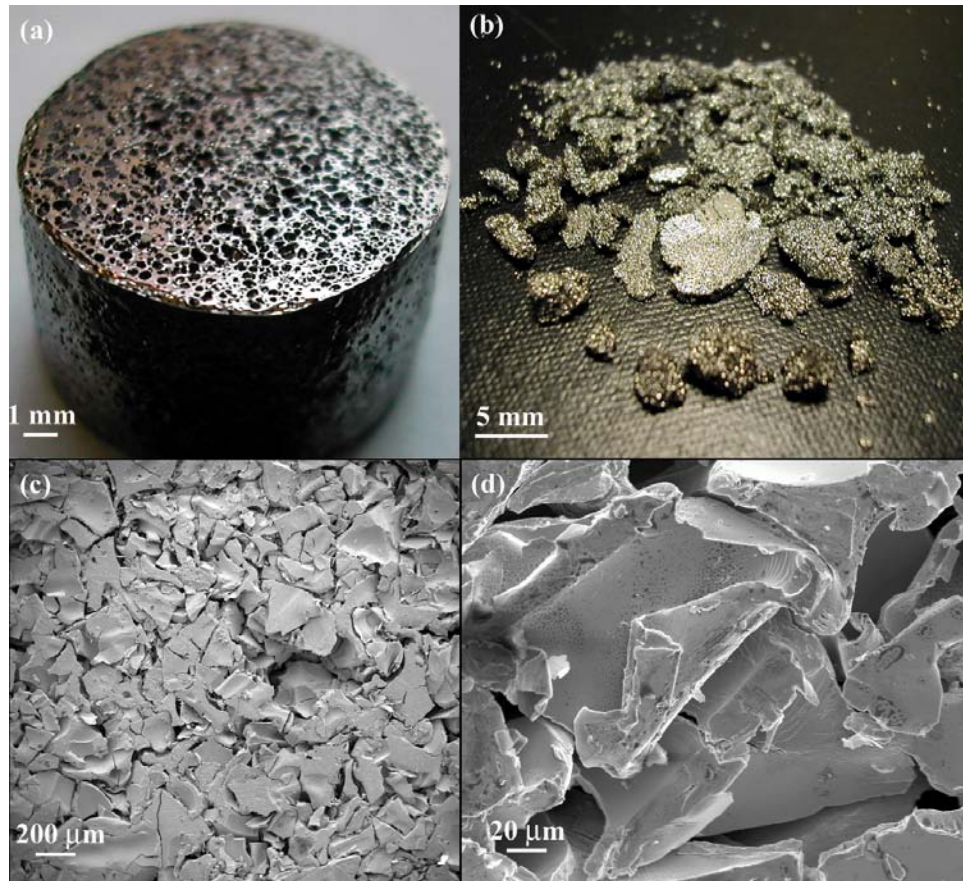


Figure 5.1: (a) Image of a foam specimen as prepared for dynamic compression. (b) Image of a foam specimen after dynamic compression showing several completely densified pieces among other crushed pieces. (c),(d) Electron micrographs of a completely densified piece of a dynamically compressed foam.

Data was reduced according to the well known equations relating the stresses and strains to the incident, reflected and transmitted strain signals [64]. Wave dispersion was also corrected, according to the guidelines of Lifshitz and Leber [65]. Finally, specimen equilibrium was carefully verified in each test by comparing the applied forces on each side of the specimen.

Results

The stress-strain response of foams loaded dynamically over a range of relative densities from 0.13 to 0.60 with applied strain rates between 3000 and 3500 s⁻¹ is presented in figure 5.2. The same general behavior is observed for all relative densities: a peak in stress is attained at approximately 0.02-0.03 strain, followed by relaxation to a rather constant stress plateau. Expectedly, as the relative density decreases, the Youngs modulus, yield stress, and plateau stress all decrease. After failure, the foam structure appears fairly fragmented. The fragments consist largely of undeformed fractured portions as well as portions that have been heavily deformed to full densification (figure 5.1(b)). Micrographs in figure 5.1(c) and (d) show one such fully densified portion from a fragmented foam specimen at low and high magnification. At high magnification (figure 5.1(d)), features including severely deformed cell walls and regions densely populated with shear bands can be seen, indicating that the struts yield plastically before or instead of fracturing. The existence of these plastically deformed features implies that plasticity may be the dominant mechanism of yielding during dynamic loading.

The quasi-static loading tests were performed over relative densities ranging between 0.22 and 0.65 and strain rates ranging between 10⁻³ and 10⁻⁴ s⁻¹. The post-yielding deformation behavior of such foams under quasi-static loading conditions has been studied extensively elsewhere [29, 35]. A typ-

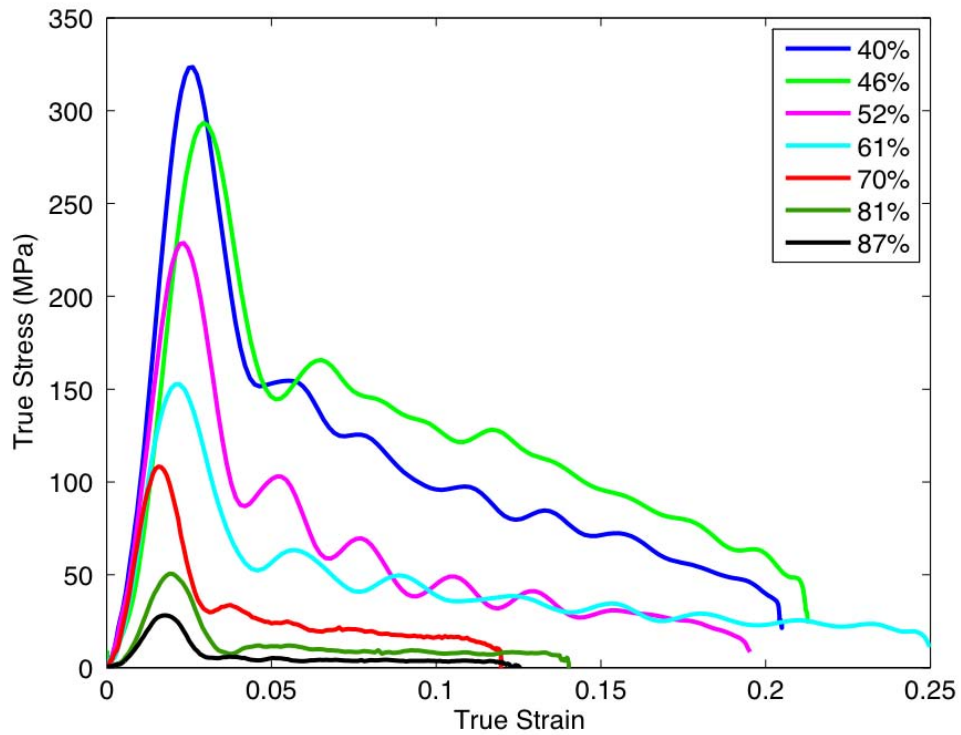


Figure 5.2: Dynamic stress-strain response of foams with varying relative densities (reported in percent porosity) under strain rates between 3000 s^{-1} and 3500 s^{-1} .

ical stress strain response of a 0.4 relative density foam deformed under a strain rate of 10^{-4} s^{-1} is shown in figure 5.3. In the same plot, we also present the stress-strain response of a specimen of equivalent relative density deformed dynamically under a strain rate of 3500 s^{-1} . The post-yielding deformation behavior for the two strain rates present some notable similarities: yielding is followed by a stress drop of about 40% towards a rough stress plateau that extends beyond 10% strain. Another interesting similarity is that yield strength for the two strain rates is nearly identical. Since monolithic amorphous metals are known to be strain-rate insensitive [13, 63], one would reasonably expect the yield strength of an amorphous metal foam to remain unchanged when the strain rate is increased from quasi-static to dynamic loading conditions. Surprisingly, the foam yield strength appears to remain unchanged with strain rate only at 40% relative density, while at other relative densities the two applied strain rates result in very different foam yield strengths.

Discussion and Conclusions

In figure 5.4 we plot the relative yield strength (foam yield strength, σ^* , normalized by the yield strength of the parent solid, σ_y , known to be 1630 MPa) [29] as a function of the relative density, ρ^*/ρ_s , for the foams tested dynamically along with those tested quasi-statically. As seen in the plot, the relative strength versus relative density data for the low and high strain rate tests fall on two distinct curves with different slopes. The two slopes in the relative strength/relative density relations point to two distinct mechanisms of yielding. That is, even though the post-yielding behavior for low and high strain rate deformation appears to be qualitatively similar (figure 5.3), the actual yielding transition (i.e., the elastic to plastic transition) appears to be

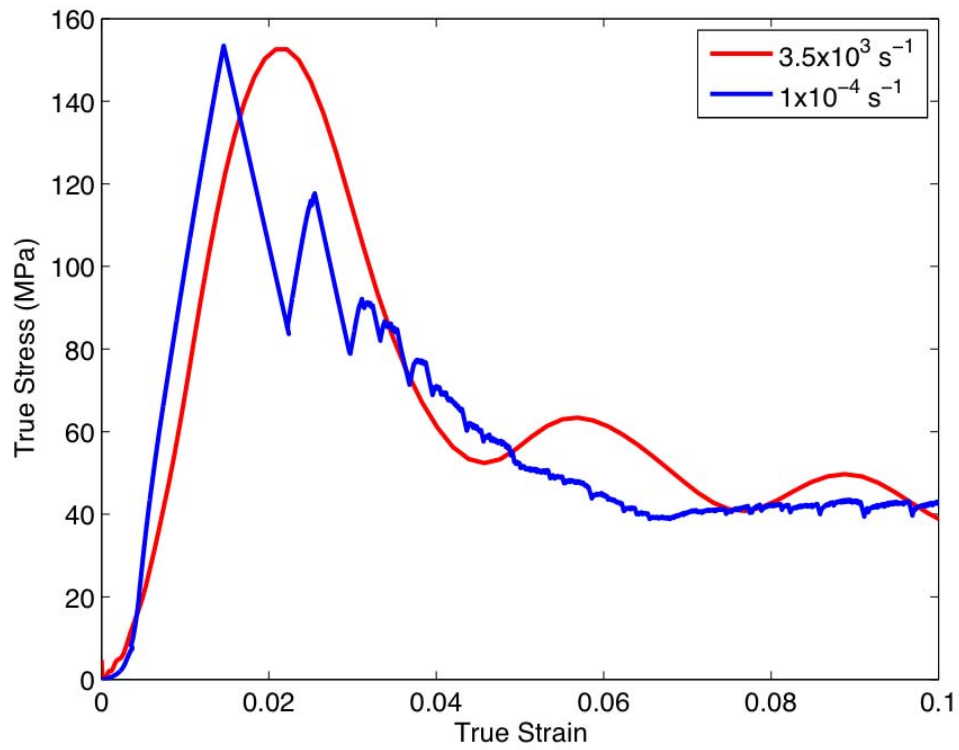


Figure 5.3: A comparison of the stress-strain response of two 60% porosity foams under applied strain rates of 3500 s^{-1} and $1 \times 10^{-4} \text{ s}^{-1}$.

fundamentally different for the two strain rate regimes. Power law fits give an exponent of 2.38 for the quasi-static data and 1.65 for the dynamic data. According to the prominent work of Gibson and Ashby [24], strength/porosity relations characterized by a power exponent of ~ 2 indicate a foam-yielding mechanism dominated by elastic buckling, while power exponents of ~ 1.5 indicate predominantly plastic yielding.

A recent in situ x-ray microtomography study [35] identified that the yielding transition of highly stochastic metallic glass foams loaded quasi-statically is indeed controlled by elastic buckling. Specifically, that study showed that yielding in such foams initiates by Eulerian buckling of high-aspect-ratio membranes distributed randomly throughout the cellular structure, and evolves by percolation of these elastic instabilities toward a non-catastrophic collapse event. The elastic yielding of quasi-statically loaded foams is therefore consistent with the relative strength/relative density power exponent of 2.38. On the other hand, the severe plastic deformation observed in the fragments of dynamically loaded foams [Fig 5.1(c) and (d)] points to a yielding mechanism dominated by plasticity, and the strength/porosity power exponent of 1.65 is also consistent with this assessment.

The strength/porosity correlations along with the observation of the yielding and failure transitions suggest that metallic glass foams with essentially self-similar cellular structures yield by distinctly different mechanisms when loaded under drastically different strain rates. Conventional metal foams, such as aluminum foams, demonstrate higher yield strengths under dynamic strain rates at a given relative density, but no apparent shift in the slope of the strength/porosity correlation (inset in figure 5.4) [66]. The higher yield strengths attained under dynamic loading can be attributed to the strain-rate sensitivity of monolithic aluminum. However the power exponent remains essentially constant with strain rate (1.4 for static and 1.6 for dynamic) which

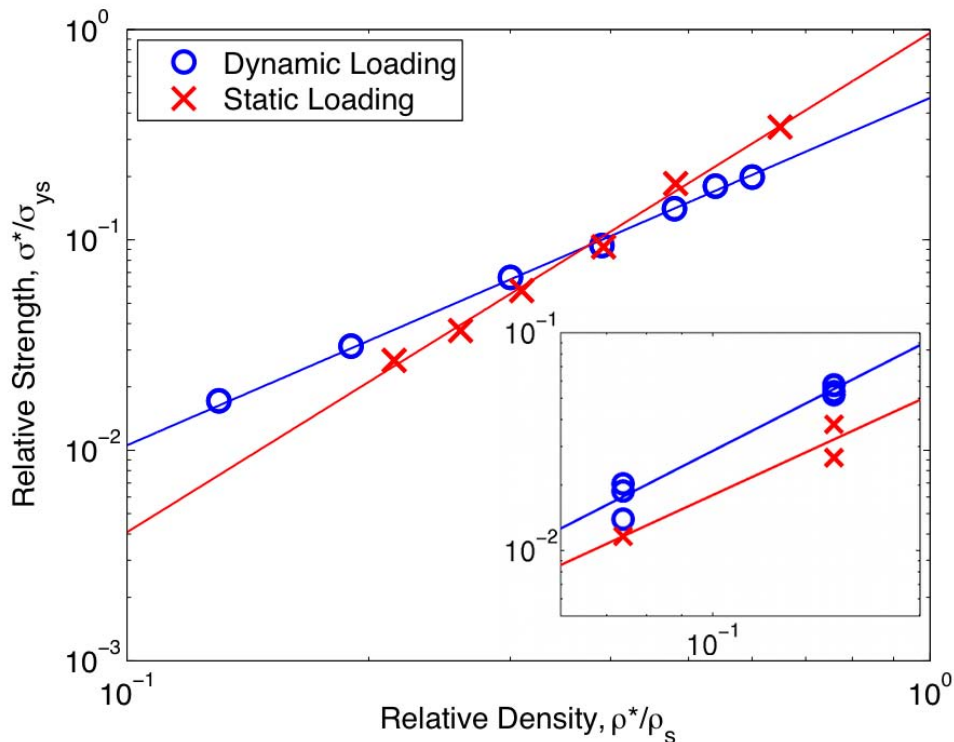


Figure 5.4: Relative strength as a function of relative density for foams tested under low and high applied strain rates. The inset shows a comparison between quasi-static ($\sim 10^{-4} \text{ s}^{-1}$) and dynamic (10^3 s^{-1}) compression of aluminum foams (Ref. [66]). Solid lines are power-law fits to the data.

suggests that the dominant yielding mechanism, which for those foams is identified to be plasticity, remains unchanged on going from quasi-static to dynamic strain rates.

The strain-rate-induced change in the foam yielding mechanism from elastic buckling to plastic yielding for the metallic glass foams investigated here can be understood by examining the mechanisms and the characteristic timescales that control them. Because of the high elastic limit of metallic glasses, a metallic glass column would generally be less stable against buckling for a given aspect ratio than a crystalline metal column. Specifically,

the critical aspect ratio that determines a column's stability against elastic buckling is given by $n\pi/\sqrt{\varepsilon_{el}}$, where ε_{el} is the elastic strain limit of the material, and the index n depends on the end constraints and ranges between 1/2 and 2 [67]. Using $\varepsilon_{el} = 0.02$ for a metallic glass column, one can estimate the critical aspect ratio to range between 20 and 40. In contrast, the critical aspect ratio for an aluminum column with $\varepsilon_{el} = 0.005$ can be estimated to range between 40 and 80. This propensity for elastic buckling forms the basis for the elastic yielding tendency of these foams, as high-aspect-ratio membranes distributed randomly throughout the cellular structure tend to buckle at critical stresses below the plastic yield stress giving rise to a global elastic yielding response [35].

As known from the work of Lindberg and Florence [68], the transient buckling response of a column to dynamic pulsed load is characterized by a timescale associated with the speed of sound in the column material. When a column is submitted to a pulsed load for duration shorter than this timescale, or equivalently, when the rate of deformation of a column exceeds this characteristic rate, the column may yield plastically before it has time to buckle elastically. To examine this concept as it pertains to this study, we define two timescales: the timescale associated with the speed of sound in the material, $\tau_{wave} = l/c$, where l is a characteristic length scale and c is the speed of sound in the material, and the timescale associated with the rate of elastic deformation, $\tau_{load} = \varepsilon_{el}/\dot{\varepsilon}$, where ε_{el} is the elastic strain limit of the material and $\dot{\varepsilon}$ is the applied strain rate. If $\tau_{load} \gg \tau_{wave}$, as in quasi-static loading, buckling would be enabled. If $\tau_{load} \geq \tau_{wave}$, as in a dynamic compression test, buckling would be suppressed. For a metallic glass membrane typical of the foams in the current study, l is on the order of the average cell size, which can be taken to be about 1 mm, $c = \sqrt{E_s/\rho_s} \approx 3200$ m/s, where $E_s \approx 100$ GPa and $\rho_s \approx 10^4$ kg/m³ are the Young's modulus and density of Pd₄₃Ni₁₀Cu₂₇P₂₀

glass, respectively, and $\varepsilon_{el} \approx 0.02$. This data give $\tau_{wave} = 3 \times 10^{-7}$ s. For a quasi-static loading test with $\dot{\varepsilon} = 10^{-4}$ s $^{-1}$ we have $\tau_{load} = 200$ s $\gg \tau_{wave}$, which implies that a stress wave could travel across the membrane many times before the plastic yield strength is reached, therefore elastic buckling would occur. For a dynamic loading test with $\dot{\varepsilon} = 10^4$ s $^{-1}$ however we have $\tau_{load} = 2 \times 10^{-6}$ s $\cong \tau_{wave}$, which implies that a membrane would reach plastic yielding as soon as the stress wave begins propagating through it, and therefore elastic buckling would be avoided.

In conclusion, microscopic analysis along with strength/porosity relations for stochastic metallic glass foams loaded dynamically reveal that dynamic yielding is controlled predominantly by plasticity, unlike quasi-static foam yielding, which is known to be dominated by elastic buckling. The strain-rate induced shift in the foam yielding mechanism is attributed to the convergence of the timescale characterizing dynamic loading and the timescale associated with sound-wave propagation across structural membranes, which thereby suppresses elastic buckling.

This work was supported in part by the MRSEC Program of the National Science Foundation under Award Number DMR-0520565.

Chapter 6

Summary and Future Directions

Summary

This thesis has been concerned with the study of the mechanical properties of amorphous metallic cellular structures. Based on the record of amorphous metal foams with high strength [36] and large plastic deformability [30], one of the goals of this work was to create amorphous metallic periodic cellular structures that would be able to outperform periodic structures made from crystalline metals. In this work periodic structures made from metallic glass and metallic glass matrix composite have been shown to inherit the impressive mechanical properties of the parent materials, and exceed them in the ability to absorb large amounts of energy while deforming to high strains without failing catastrophically. These structures also outperform the current state-of-the-art stainless steel structures of the same general geometry in strength and energy absorption.

Amorphous metal foams produced by a powder metallurgy route have been investigated, showing high yield strengths corresponding to plastic yielding of cell walls and energy absorption higher than other metallic glass foams. Another type of amorphous metal foam known to yield by elastic buckling of cell walls [35] was tested under two disparate strain rates and a change

in the yield mechanism was observed upon a drastic increase in strain rate. This mechanism change has been explained as the result of the rate of the mechanical test approaching or even eclipsing the speed of elastic waves in the material.

Future Direction in BMG and MGMC Honeycombs

The strength capabilities and energy absorption capabilities of metallic glass and metallic glass matrix composite honeycombs have been shown here. In future work, it would be useful to devise a method or an apparatus that could produce periodic sheets of MGMC with higher porosity to fill in the lack of low relative density data points for these structures. Thinner struts would be one way to do this which might result in these MGMC structures deforming to densification with fewer collapse events. Another way to reduce the density is to change the geometry of the structure to a less dense one. One example of a more porous structure is the egg-box structure which was investigated in chapter 3. Other more porous structures that could be made from these materials are the three-dimensional structures that are made from connected columns and not connected plates of the parent material. Two examples of this type of structure are the textile and the truss, examples of which are shown in Fig. 6.1.

Two major issues with these structures are bonding and uniformity of cellular elements. Cellular structures are commonly used as the core of sandwich panels, and the cores must be bonded to the face sheets of the sandwich and to each other in the case of corrugated sheets used to make a honeycomb. Metallic glasses are difficult to bond together without risking crystallization, but several methods have been studied. Among these methods are laser weld-

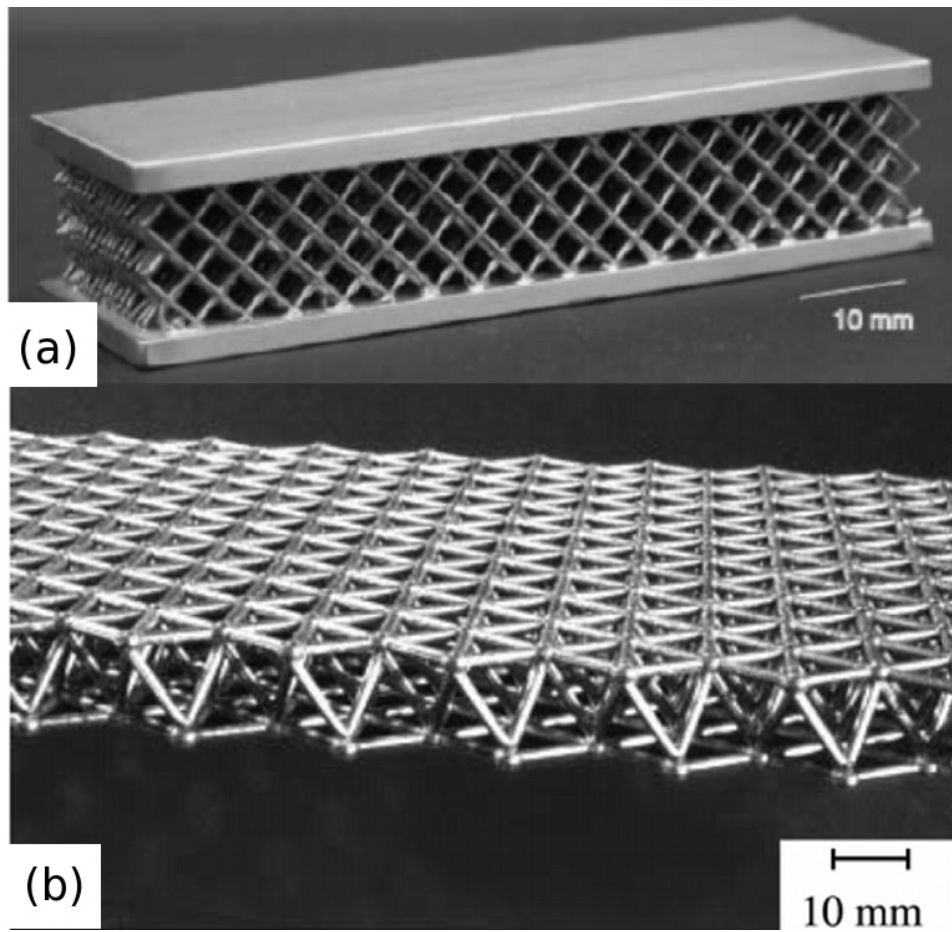


Figure 6.1: Examples of crystalline metal (a) textile and (b) truss.

ing [69, 70], consolidation using electrical discharge welding [71], and adhesive bonding using a cured sol gel layer between metallic glass and epoxy [72]. This final method is interesting because it uses the chemistry of the cured sol gel layer and not local heating of the material to make the bond. Any of these methods could be quite promising for both BMG and MGMC structures if joining can occur without harming the amorphous nature of the material and the bond is strong enough to remain intact as the material around it yields. When the elements of the cellular structure are not uniform, the stochasticity of the structure affects its strength and energy absorbing capabilities as thinner elements may yield early in the deformation plastically or by buckling, and thicker elements may have limited plastic deformability ending in fracture causing a collapse event in the structure. Ideally, the elements of a structure should be uniformly thin.

For any of these structures, it would be desirable to be able to make them in a shorter amount of time so that the sample heating and forming have as small an effect as possible on the amorphous nature of the glass-forming alloy. Containerless processing would also be desirable as the glassy liquid is quite reactive at elevated temperatures. For MGMC structures, the current method involves induction heating in an argon atmosphere, which is basically containerless, but only heats the skin of the sample directly and the rest of the sample is heated by thermal conduction. Forging is currently done manually by the operator plunging the top die into the semi-solid material. An automated system may be able to heat the composite more quickly and uniformly and would definitely produce more uniform parts with thinner struts. For the BMG sheets, it is desirable to process in the supercooled liquid region. A method involving rapid heating from the amorphous state followed by rapid forming and quenching is in development in the Johnson group. This method involves the heating of a metallic glass using the discharge of

capacitors and forming in a matter of milliseconds. At these heating, forming, and cooling rates, the glass will not have time to crystallize or react with its surroundings before it has been quenched to room temperature.

The true laboratory test of any energy absorbing structure is a dynamic impact test. Future research on metallic glass and metallic glass matrix composites should include dynamic impact testing of some type. It would be quite interesting to find out whether the phenomenon of elastic buckling suppression observed in chapter 5 is present in very porous periodic honeycomb or egg-box structures.

Conclusion

Amorphous metallic cellular structures have impressive mechanical properties that can surpass those for structures made of crystalline metals despite some non-optimized aspects. The structures tested in this thesis are not completely optimized for strength or energy absorption as a multi-level structure or as sandwich panels because of the lack of reliable bonding and non-uniformity of the structural elements. There are ways to fix these problems, though, and ideal structures made from metallic glasses and metallic glass matrix composites could be even more impressive than those exhibited in this thesis.

Bibliography

- [1] W Klement, RH Willens, and P Duwez. Non-crystalline structure in solidified gold-silicon alloys. *Nature*, 187(4740):869–870, 1960.
- [2] HS Chen and D Turnbull. Formation, stability and structure of palladium-silicon based alloy glasses. *Acta Metallurgica*, 17(8):1021–1031, 1969.
- [3] A Inoue, T Zhang, and T Masumoto. Glass-forming ability of alloys. *Journal of Non-Crystalline Solids*, 156(8):473–480, 1993.
- [4] A Inoue, N Nishiyama, and T Matsuda. Preparation of bulk glassy Pd₄₀Ni₁₀Cu₃₀P₂₀ alloy of 40 mm in diameter by water quenching. *Materials Transactions JIM*, 37(2):181–184, 1996.
- [5] A Peker and WL Johnson. A highly processable metallic glass—Zr_{41.2}Ti_{13.8}Cu_{12.5}Ni_{10.0}Be_{22.5}. *Applied Physics Letters*, 63(17):2342–2344, 1993.
- [6] CC Hays, CP Kim, and WL Johnson. Large supercooled liquid region and phase separation in the Zr-Ti-Ni-Cu-Be bulk metallic glasses. *Applied Physics Letters*, 75(8):1089–1091, 1999.
- [7] D Turnbull. Under what conditions can a glass be formed? *Contemporary Physics*, 10(5):473–488, 1969.

- [8] DW Suh and RH Dauskardt. Mechanical relaxation time scales in a Zr-Ti-Ni-Cu-Be bulk metallic glass. *Journal of Materials Research*, 17(6):1254–1257, 2002.
- [9] J Schroers and WL Johnson. Extremely low critical cooling rate measured on dispersed $\text{Pd}_{43}\text{Ni}_{10}\text{Cu}_{27}\text{P}_{20}$. *Applied Physics Letters*, 80(12):2069–2071, 2002.
- [10] J Schroers, WL Johnson, and Ralf Busch. Crystallization kinetics of the bulk-glass-forming $\text{Pd}_{43}\text{Ni}_{10}\text{Cu}_{27}\text{P}_{20}$ melt. *Applied Physics Letters*, 77(8):1158–1160, 2000.
- [11] A Inoue, N Nishiyama, and H Kimura. Preparation and thermal stability of bulk amorphous $\text{Pd}_{40}\text{Cu}_{30}\text{Ni}_{10}\text{P}_{20}$ alloy cylinder of 72 mm in diameter. *Materials Transactions JIM*, 38(2):179–183, 1997.
- [12] MF Ashby and AL Greer. Metallic glasses as structural materials. *Scripta Materialia*, 54(3):321–326, 2006.
- [13] HA Bruck, AJ Rosakis, and WL Johnson. The dynamic compressive behavior of beryllium bearing bulk metallic glasses. *Journal of Materials Research*, 11(2):503–511, 1996.
- [14] JJ Lewandowski, WH Wang, and AL Greer. Intrinsic plasticity or brittleness of metallic glasses. *Philosophical Magazine Letters*, 85(2):77–87, 2005.
- [15] J Schroers and WL Johnson. Ductile bulk metallic glass. *Physical Review Letters*, 93(25):255506, 2004.
- [16] RD Conner, WL Johnson, NE Paton, and WD Nix. Shear bands and cracking of metallic glass plates in bending. *Journal of Applied Physics*, 94(2):904–911, 2003.

- [17] RD Conner, Y Li, WD Nix, and WL Johnson. Shear band spacing under bending of Zr-based metallic glass plates. *Acta Materialia*, 52(8):2429–2434, 2004.
- [18] WL Johnson. Bulk glass-forming metallic alloys: Science and technology. *MRS Bulletin*, 24(10):42–56, 1999.
- [19] G Duan, ML Lind, K De Blauwe, A Wiest, and WL Johnson. Thermal and elastic properties of Cu-Zr-Be bulk metallic glass forming alloys. *Applied Physics Letters*, 90(21):211901, 2007.
- [20] G Duan, K De Blauwe, ML Lind, JP Schramm, and WL Johnson. Compositional dependence of thermal, elastic, and mechanical properties in Cu-Zr-Ag bulk metallic glasses. *Scripta Materialia*, 58(3):159–162, 2008.
- [21] X Gu, A McDermott, S Poon, and G Shiflet. Critical Poisson’s ratio for plasticity in Fe–Mo–C–B–Ln bulk amorphous steel. *Applied Physics Letters*, 88:211905, 2006.
- [22] CC Hays, CP Kim, and WL Johnson. Improved mechanical behavior of bulk metallic glasses containing in situ formed ductile phase dendrite dispersions. *Materials Science and Engineering A*, 304:650–655, 2001.
- [23] DC Hofmann, J-Y Suh, A Wiest, G Duan, ML Lind, MD Demetriou, and WL Johnson. Designing metallic glass matrix composites with high toughness and tensile ductility. *Nature*, 451(7182):1085–U3, 2008.
- [24] Lorna J. Gibson and Michael F. Ashby. *Cellular Solids : Structure & Properties*. Cambridge, UK:Cambridge University Press, 2nd edition, 1997.
- [25] MF Ashby. The mechanical properties of cellular solids. *Metallurgical Transactions A*, 14(9):1755–1769, 1983.

- [26] JG Davies and S Zhen. Metallic foams: Their production, properties and applications. *Journal of Materials Science*, 18(7):1899–1911, 1983.
- [27] BT Bhat and TG Wang. A comparison of mechanical properties of some foams and honeycombs. *Journal of Materials Science*, 25(12):5157–5162, 1990.
- [28] J Schroers, C Veazey, and WL Johnson. Amorphous metallic foam. *Applied Physics Letters*, 82(3):370–372, 2003.
- [29] T Wada and A Inoue. Formation of porous Pd-based bulk glassy alloys by a high hydrogen pressure melting–water quenching method and their mechanical properties. *Materials Transactions JIM*, 45(8):2761–2765, 2004.
- [30] AH Brothers and DC Dunand. Ductile bulk metallic glass foams. *Advanced Materials*, 17(4):484–486, 2005.
- [31] AH Brothers and DC Dunand. Syntactic bulk metallic glass foam. *Applied Physics Letters*, 84(7):1108–1110, 2004.
- [32] MH Lee and DJ Sordélet. Nanoporous metallic glass with high surface area. *Scripta Materialia*, 55(10):947–950, 2006.
- [33] XH Chen, Y Zhang, XC Zhang, XD Hui, BC Wei, and GL Chen. A porous bulk metallic glass with unidirectional opening pores. *Electrochemical and Solid State Letters*, 10(12):E21–E23, 2007.
- [34] AH Brothers and DC Dunand. Plasticity and damage in cellular amorphous metals. *Acta Materialia*, 53(16):4427–4440, 2005.
- [35] MD Demetriou, JC Hanan, C Veazey, M Di Michiel, N Lenoir, E Üstündag, and WL Johnson. Yielding of metallic glass foam by

- percolation of an elastic buckling instability. *Advanced Materials*, 19(15):1957–1962, 2007.
- [36] MD Demetriou, C Veazey, JS Harmon, JP Schramm, and WL Johnson. Stochastic metallic-glass cellular structures exhibiting benchmark strength. *Physical Review Letters*, 101(14):145702, 2008.
- [37] J Schroers, Q Pham, A Peker, N Paton, and RV Curtis. Blow molding of bulk metallic glass. *Scripta Materialia*, 57(4):341–344, 2007.
- [38] MH Lee, DH Bae, WT Kim, DH Kim, E Rozhkova, PB Wheelock, and DJ Sordélet. Synthesis of Ni-based bulk amorphous alloys by warm extrusion of amorphous powders. *Journal of Non-Crystalline Solids*, 315(1–2):89–96, 2003.
- [39] MD Demetriou, C Veazey, J Schroers, JC Hanan, and WL Johnson. Thermo-plastic expansion of amorphous metallic foam. *Journal of Alloys and Compounds*, 434–435:92–96, 2007.
- [40] A Wiest, G Duan, MD Demetriou, LA Wiest, A Peck, G Kaltenboeck, B Wiest, and WL Johnson. Zr-Ti-based Be-bearing glasses optimized for high thermal stability and thermoplastic formability. *Acta Materialia*, 56(11):2625–2630, 2008.
- [41] A Wiest, JS Harmon, MD Demetriou, RD Conner, and WL Johnson. Injection molding metallic glass. *Scripta Materialia*, 60(3):160–163, 2009.
- [42] AH Brothers and DC Dunand. Porous and foamed amorphous metals. *MRS Bulletin*, 32(8):639–643, 2007.
- [43] MH Lee and DJ Sordélet. Synthesis of bulk metallic glass foam by powder extrusion with a fugitive second phase. *Applied Physics Letters*, 89(2):021921, 2006.

- [44] T Wierzbicki. Crushing analysis of metal honeycombs. *International Journal of Impact Engineering*, 1(2):157–174, 1983.
- [45] Jin-Yoo Suh. *Fracture toughness study on bulk metallic glasses and novel joining method using bulk metallic glass solder*. PhD thesis, California Institute of Technology, 2009.
- [46] F Côté, VS Deshpande, NA Fleck, and AG Evans. The compressive and shear responses of corrugated and diamond lattice materials. *International Journal of Solids and Structures*, 43(20):6220–6242, 2006.
- [47] F Côté, VS Deshpande, NA Fleck, and AG Evans. The out-of-plane compressive behavior of metallic honeycombs. *Materials Science and Engineering A*, 380(1-2):272–280, 2004.
- [48] DC Hofmann, J-Y Suh, A Wiest, ML Lind, MD Demetriou, and WL Johnson. Development of tough, low-density titanium-based bulk metallic glass matrix composites with tensile ductility. *Proceedings of the National Academy of Sciences*, 105(51):20136–20140, 2008.
- [49] CC Hays, CP Kim, and WL Johnson. Microstructure controlled shear band pattern formation and enhanced plasticity of bulk metallic glasses containing in situ formed ductile phase dendrite dispersions. *Physical Review Letters*, 84(13):2901–2904, 2000.
- [50] SY Lee, CP Kim, JD Almer, U Lienert, E Üstündag, and WL Johnson. Pseudo-binary phase diagram for Zr-based in situ beta phase composites. *Journal of Materials Research*, 22(2):538–543, 2007.
- [51] DC Hofmann, H Kozachkov, HE Khalifa, JP Schramm, MD Demetriou, KS Vecchio, and WL Johnson. Semi-solid induction forging of metallic glass matrix composites. *JOM*, in press.

- [52] DC Hofmann, J-Y Suh, A Wiest, and WL Johnson. New processing possibilities for highly toughened metallic glass matrix composites with tensile ductility. *Scripta Materialia*, 59(7):684–687, 2008.
- [53] WL Johnson. Bulk amorphous metal—an emerging engineering material. *JOM*, 54(3):40–43, 2002.
- [54] J Schroers. The superplastic forming of bulk metallic glasses. *JOM*, 57(5):35–39, 2005.
- [55] J Schroers and N Paton. Amorphous metal alloys form like plastics. *Advanced Materials & Processes*, 164(11):61–63, 2006.
- [56] J Schroers, C Veazey, MD Demetriou, and WL Johnson. Synthesis method for amorphous metallic foam. *Journal of Applied Physics*, 96(12):7723–7730, 2004.
- [57] MD Demetriou, C Veazey, J Schroers, JC Hanan, and WL Johnson. Expansion evolution during foaming of amorphous metals. *Materials Science and Engineering A*, 449:863–867, 2007.
- [58] Y Kawamura, H Kato, A Inoue, and T Masumoto. Fabrication of bulk amorphous alloys by powder consolidation. *International Journal of Powder Metallurgy*, 33(22):50–61, 1997.
- [59] DH Bae, MH Lee, DH Kim, and DJ Sordellet. Plasticity in $\text{Ni}_{59}\text{Zr}_{20}\text{Ti}_{16}\text{Si}_2\text{Sn}_3$ metallic glass matrix composites containing brass fibers synthesized by warm extrusion of powders. *Applied Physics Letters*, 83(12):2312–2314, 2003.
- [60] T Wada, X Wang, H Kimura, and A Inoue. Preparation of a Zr-based bulk glassy alloy foam. *Scripta Materialia*, 59(10):1071–1074, 2008.

- [61] AH Brothers and DC Dunand. Amorphous metal foams. *Scripta Materialia*, 54(4):513–520, 2006.
- [62] MD Demetriou, G Duan, C Veazey, K De Blauwe, and WL Johnson. Amorphous Fe-based metal foam. *Scripta Materialia*, 57(1):9–12, 2007.
- [63] T Mukai, TG Nieh, Y Kawamura, A Inoue, and K Higashi. Dynamic response of a Pd₄₀Ni₄₀P₂₀ bulk metallic glass in tension. *Scripta Materialia*, 46(1):43–47, 2002.
- [64] Herbert Kolsky. *Stress Waves in Solids*. Dover Publications, New York, 1963.
- [65] JM Lifshitz and H Leber. Data-Processing in the Split Hopkinson Pressure Bar Tests. *International Journal of Impact Engineering*, 15(6):723–733, 1994.
- [66] KA Dannemann and J Lankford. High strain rate compression of closed-cell aluminium foams. *Materials Science and Engineering A*, 293(1-2):157–164, 2000.
- [67] James M. Gere and Stephen P. Timoshenko. *Mechanics of Materials*. Boston : PWS-Kent, 3rd ed. edition, 1975. Ch. 9.
- [68] Herbert E. Lindberg and Alexander L. Florence. *Dynamic pulse buckling : theory and experiment*. Dordrecht, Boston : M. Nijhoff, 1987.
- [69] Y Kawahito, T Terajima, H Kimura, T Kuroda, K Nakata, S Katayama, and A Inoue. High-power fiber laser welding and its application to metallic glass Zr₅₅Al₁₀Ni₅Cu₃₀. *Materials Science and Engineering B*, 148(1-3):105–109, 2008.

- [70] JH Kim, C Lee, DM Lee, JH Sun, SY Shin, and JC Bae. Pulsed Nd : Yag laser welding of $\text{Cu}_{54}\text{Ni}_6\text{Zr}_{22}\text{Ti}_{18}$ bulk metallic glass. *Materials Science and Engineering A*, 449:872–875, 2007.
- [71] YW Kim, DL Bourell, and C Persad. Consolidation of metallic-glass ribbons using electric-discharge welding. *Metallurgical Transactions A*, 19(6):1634–1638, 1988.
- [72] R Dauskardt. Personal communication, 2008.